*Revision for Geochimica et Cosmochimica Acta*

*Manuscript W5271*

# Weathering of the Rio Blanco quartz diorite, Luquillo Mountains, Puerto Rico: Coupling oxidation, dissolution, and fracturing

**Heather L. Buss[1,*], Peter B. Sak[2], Samuel M. Webb[3], and Susan L. Brantley[4]**

[1]U.S. Geological Survey, 345 Middlefield Road, MS 420, Menlo Park, CA, 94025 USA (hlbuss@usgs.gov)

[2]Department of Geology, Dickinson College, Carlisle, PA, 17013 USA (sakp@dickinson.edu)

[3]Stanford Synchrotron Radiation Laboratory, Stanford Linear Accelerator Center, 2525 Sand Hill Road, MS 69, Menlo Park, CA, 94025 USA (samwebb@slac.stanford.edu)

[4]Earth and Environmental Systems Institute, Penn State University, University Park, PA, 16802 USA (brantley@eesi.psu.edu)

May 29, 2008

[*] Corresponding author

# Abstract

In the mountainous Rio Icacos watershed in northeastern Puerto Rico, quartz diorite bedrock weathers spheroidally, producing a 0.2-2 m thick zone of partially weathered rock layers (~2.5 cm thickness each) called rindlets, which form concentric layers around corestones. Spheroidal fracturing has been modeled to occur when a weathering reaction with a positive $\Delta V$ of reaction builds up elastic strain energy. The rates of spheroidal fracturing and saprolite formation are therefore controlled by the rate of the weathering reaction.

Chemical, petrographic, and spectroscopic evidence demonstrates that biotite oxidation is the most likely fracture-inducing reaction. This reaction occurs with an expansion in d (001) from 10.0 to 10.5 Å, forming "altered biotite". Progressive biotite oxidation across the rindlet zone was inferred from thin sections and gradients in K and Fe(II). Using the gradient in Fe(II) and constraints based on cosmogenic age dates, we calculated a biotite oxidation reaction rate of $8.2 \times 10^{-14}$ mol biotite $m^{-2}$ $s^{-1}$. Biotite oxidation was documented within the bedrock corestone by synchrotron X-ray microprobe fluorescence imaging and XANES. X-ray microprobe images of Fe(II) and Fe(III) at 2 μm resolution revealed that oxidized zones within individual biotite crystals are the first evidence of alteration of the otherwise unaltered corestone.

Fluids entering along fractures lead to the dissolution of plagioclase within the rindlet zone. Within 7 cm surrounding the rindlet-saprolite interface, hornblende dissolves to completion at a rate of $6.3 \times 10^{-13}$ mol hornblende $m^{-2}$ $s^{-1}$: the fastest reported rate of hornblende weathering in the field. This rate is consistent with laboratory-derived hornblende dissolution rates. By revealing the coupling of these mineral weathering reactions to fracturing and porosity formation we are able to describe the process by which the quartz diorite bedrock disaggregates

47 and forms saprolite. In the corestone, biotite oxidation induces spheroidal fracturing, facilitating
48 the influx of fluids that react with other minerals, dissolving plagioclase and chlorite, creating
49 additional porosity, and eventually dissolving hornblende and precipitating secondary minerals.
50 The thickness of the resultant saprolite is maintained at steady state by a positive feedback
51 between the denudation rate and the weathering advance rate driven by the concentration of pore
52 water $O_2$ at the bedrock-saprolite interface.

53 **1. INTRODUCTION**

54 Rock weathering is the initial step in the soil-forming process and the primary contributor
55 of chemical solutes to the hydrosphere. The boundaries at which weathering transforms intact
56 bedrock into disaggregated regolith (such as saprolite) are complex interfaces controlled by
57 coupled chemical, physical, and microbial processes driven by the flux of reactants into the
58 bedrock. The rate of rock weathering determines the advance rate of the bedrock-saprolite
59 interface and, in a steady state profile, the rate of formation of soil. In turn, the rates of individual
60 geochemical reactions contribute to the bedrock weathering rate, the flux of mineral nutrients to
61 the biosphere, and the flux of solutes to the hydrosphere.
62 Soils developed on granite, sandstone, and metamorphosed crystalline bedrock have often
63 been presumed to be in steady state with respect to thickness (e.g., Brown et al., 1995; Heimsath
64 et al., 1999; von Blanckenburg et al., 2004), regolith formation, erosion, weathering (e.g.,
65 Pavich, 1989; Brown et al., 1995; Riebe et al., 2003; Turner et al., 2003; Dosseto et al., Subm.),
66 elemental concentrations (e.g., Riebe et al., 2003), and yearly-averaged biomass and organic
67 carbon (Buss et al., 2005). If indeed the total mass of regolith (including saprolite) in a profile is

68 constant in time, then conservation of mass requires that the rate of formation of regolith equals
69 the total denudation rate, and thus the sum of the rates of chemical weathering and physical
70 erosion. In an isovolumetric weathering profile (such as a saprolite), steady state mass is
71 equivalent to steady state thickness. In the granitic Rio Icacos watershed in Puerto Rico, Brown
72 et al. (1995) estimated a long-term average total denudation rate of 43 m $Ma^{-1}$ ± 35% based on
73 cosmogenic $^{10}Be$ accumulations in the stream sediments, consistent with later estimates by White
74 et al. (1998) and Riebe et al. (2003) using combinations of cosmogenic nuclide and geochemical
75 mass balance methods. White et al. (1998) calculated the rate of regolith formation (also known
76 as the *weathering advance rate*) as 58 m $Ma^{-1}$ based on the watershed solute flux normalized to
77 the geographical surface area (expressed as unit regolith surface area). The agreement of these
78 rates supports the assumption of a steady state regolith profile. Thus, the total denudation rate is
79 commonly equated with the rate of bedrock transformation to regolith for the Rio Icacos
80 watershed and other sites where weathering is assumed to be occurring at steady state (e.g.,
81 Murphy et al., 1998; White et al., 1998; Riebe et al., 2003; Turner et al., 2003; Buss et al., 2005;
82 Fletcher et al., 2006).

83 Although steady state assumptions are frequently used in models the coupling between
84 erosion and weathering advance rates is difficult to understand. Fletcher et al. (2006) proposed
85 that the rate at which saprolite is created from the Rio Icacos bedrock is controlled by the
86 chemistry of pore fluids at depth and that this chemistry is in turn controlled by the thickness of
87 the regolith profile. Pore fluid $O_2$ may diffuse into the bedrock, oxidizing Fe(II)-bearing primary
88 minerals, creating elastic strain that spheroidally fractures the Rio Icacos bedrock (Fletcher et al.,
89 2006). In many locations such as Rio Icacos, bedrock disaggregates to regolith at spheroidally
90 weathering interfaces. Geochemical reactions involving Fe-silicate minerals have been credited

with causing the fracturing that initiates regolith formation at such interfaces (e.g., Larsen, 1948; Simpson, 1964; Eggler et al., 1969; Isherwood and Street, 1976; Chatterjee and Raymahashay, 1998; Scarciglia et al., 2005; Fletcher et al., 2006).

Fletcher et al. (2006) proposed that oxidation of hornblende (where $\Delta V_{reaction} > 0$) drives fracturing and controls the rate of weathering advance. Given that dissolved $O_2$ in soil pore waters decreases with depth, they pointed out that deeper soils would have slower weathering advance rates than shallower soils. Their model is consistent with pore water dissolved $O_2$ as the parameter that couples erosion to the weathering advance rate. Herein we present a detailed geochemical investigation of the spheroidally weathering bedrock-saprolite interface in the Rio Icacos watershed. Specifically we examine the occurrence and rates of individual mineral weathering reactions within the spheroidally fractured zone, with particular emphasis on the Fe-silicate minerals, in order to identify the fracture-initiating reaction, to understand the relationships between specific reactions and porosity development, and to quantify the flux of Fe(II) from weathering bedrock.

### 1.1. Spheroidal Weathering

Spheroidal weathering refers to a well known but poorly understood type of exfoliation in which corestones are surrounded by concentric layers of weathering rock (Ollier, 1971). Corestones are blocks of residual bedrock that are weathered in place along pre-existing joint planes, rounding off corners to create boulders (Linton, 1955; Ollier, 1971). The concentric layers surrounding corestones are variously called sheets, layers, shells, plates, scales, or rindlets (Bisdom, 1967; Ollier, 1971; Fritz and Ragland, 1980). Envisioning an entire sequence of layers

112 as a weathering rind, here we adopt the term rindlets to describe the individual layers consistent
113 with terminology used by Fritz and Ragland (1980), Turner et al. (2003), Buss et al. (2005), and
114 Fletcher et al. (2006). We also refer to a complete set of rindlets as a rindlet zone (Figures 1-2).
115 Spheroidal weathering is most common in homogeneous, jointed, competent rocks,
116 primarily granite and basalt although it has also been observed on gneisses, schists, andesites,
117 sandstones, and greywackes (e.g., Ollier, 1967; Heald et al., 1979; Fritz and Mohr, 1984;
118 Chatterjee and Raymahashay, 1998). Granitic corestones are found in a variety of climatic
119 regions on all continents except Antarctica and thus represent a widespread phenomenon
120 impacting regolith formation worldwide.
121 Large-scale exfoliation structures such as tors or domes in the Sierra Nevada have long
122 been thought to be created by the dilation induced by the relief of stress during erosional
123 unloading (e.g., Gilbert, 1904; Farmin, 1937; Schattner, 1961; Thomas, 1974), a mechanism
124 thought to be independent of – although aggravated by – surficial processes such as hydration
125 and freeze-thaw (e.g., Farmin, 1937). Spheroidal weathering has often been recognized as a
126 different, or special, case of exfoliation and has been attributed to surficial processes, most
127 commonly chemical weathering (Farmin, 1937; Ollier, 1971; Fletcher et al., 2006). It is unclear
128 why some rocks weather spheroidally and others do not. Some investigators have proposed that
129 the percentage of biotite (Le Pera and Sorriso-Valvo, 2000) or feldspar (Ferry, 1984) controls
130 susceptibility to spheroidal weathering and others have argued for (Isherwood and Street, 1976;
131 Sequeira Braga et al., 2002) or against (Ollier, 1988; Romani and Twidale, 1998; Mignon and
132 Thomas, 2002) climatic controls. A number of researchers have suggested that dilation during
133 mineral weathering could induce spheroidal fracturing or fracture-induced disintegration (e.g.,
134 Larsen, 1948; Simpson, 1964; Eggler et al., 1969; Isherwood and Street, 1976; Begle, 1978;

135 Bustin and Mathews, 1979; Chatterjee and Raymahashay, 1998; Fletcher et al., 2006). Ollier
136 (1967) argues that a net volume change is unlikely because the rocks retain joint and mineral
137 structure after spheroidal cracking. Indeed, spheroidal weathering often produces saprolite,
138 which is defined as an isovolumetric weathering product. Fletcher et al. (2006) demonstrated
139 quantitatively that only a very small net volume change is required to generate a build-up of
140 elastic strain energy sufficient to produce the fractures that define individual rindlets.

141 Fletcher et al. (2006) postulated that a positive $\Delta V_{reaction}$ ($\Delta V_{reaction} = \Sigma V_{products} -$
142 $\Sigma V_{reactants}$) for the precipitation of ferric oxides after the oxidation of ferrous minerals builds-up
143 elastic strain energy in the rock, which causes the fracturing that demarcates rindlets. In this
144 scenario, the rate of spheroidal weathering, and hence the rate of advance of the bedrock-
145 saprolite interface (the rindlet zone), is a function of the concentrations of ferrous minerals and
146 oxygen, the reaction rate, the rate of transport, and the mechanical properties of the rock.
147 Fletcher et al. (2006) proposed that the dissolution of hornblende in a granitic rock coupled with
148 a precipitation of ferrihydrite could yield a positive $\Delta V_{reaction}$. However, there are several possible
149 reactions involving ferrous minerals common to granitic rocks that could produce a ferric
150 product: dissolution of hornblende, biotite, or augite followed by precipitation of a ferric
151 (hydr)oxide mineral, or solid-phase oxidation of Fe(II) within hornblende, biotite, or augite. In
152 the present paper we seek to identify the first weathering reaction that occurs in the corestones in
153 order to refine the model presented in Fletcher et al. (2006) and to identify controls on the
154 thickness of the rindlet zone and its transformation to saprolite.

155 In a spheroidally weathering system, a rindlet sequence defines the bedrock-saprolite
156 interface, where bedrock chemically weathers and disaggregates to form saprolite (Figure 2). For
157 an assumed steady-state system such as the Rio Icacos weathering profile (Brown et al., 1995;

158 Riebe et al., 2003; Fletcher et al., 2006), the rate of formation of the saprolite is equal to the
159 movement of the boundary between the saprolite and the bedrock and to the total denudation
160 rate. This boundary moves downward into the bedrock as rindlets form during spheroidal
161 weathering. Turner et al. (2003) conceptualized the Rio Icacos weathering profile as multiple
162 parallel weathering fronts that advance inward towards the center of the corestones as well as
163 inward from inter-rindlet boundaries towards the rindlet centers. In this model, the net rate of
164 advance of the multiple rindlet-scale fronts equals the net rate of advance of the corestone-scale
165 front. Likewise, the net rate of advance of the corestone-scale front equals the total denudation
166 rate. If the rindlet-bounding fractures are a series of parallel weathering fronts (as per Turner et
167 al., 2003), then chemical and mineralogical trends should be measurable across a single rindlet.
168 That is, weathering intensity should decrease markedly from a rindlet's edges towards the
169 rindlet's interior. In this case, the weathering advance rate would be the sum of the rates of the
170 individual parallel rindlet fronts. Alternatively, the entire rindlet zone could be a single
171 weathering front with only two controlling interfaces: the bedrock-rindlet interface and the
172 rindlet-saprolite interface (Figure 2).

173 **1.2. Field Site and Sample Collection**

174 The Rio Icacos watershed in Puerto Rico's Luquillo Experimental Forest is located on
175 Rio Blanco quartz diorite bedrock mantled by 200 ka regolith, which was dated using $^{10}$Be
176 (Brown et al., 1995). The regolith is composed of 2-8 m of saprolite and 0.5-1 m of soil. These
177 Picacho-Ciales complex soils, previously classified as ultisols (Boccheciamp et al., 1977), are
178 now considered inceptisols due to weak B horizon development, despite being highly weathered

179 (USDA NCRS, 2002). The quartz diorite weathers spheroidally forming corestones that average
180 2 m in diameter, surrounded by 0.2-2 m rindlet zones containing individual rindlets of 2.6 cm
181 average thickness (Turner et al., 2003; Buss et al., 2004; Buss et al., 2005; Fletcher et al., 2006).
182 The Rio Blanco quartz diorite bedrock contains zoned plagioclase, quartz, hornblende,
183 partially chloritized biotite, and minor primary iron oxides and accessory minerals (Murphy et
184 al., 1998; White et al., 1998). The overlying saprolite contains kaolinite, goethite, quartz, and
185 biotite. Biotite weathering occurs in two stages via two mechanisms. First, an "altered biotite"
186 phase forms that has a larger d (001) spacing, and higher Al/Si and Fe(III)/Fe(II) ratios, and less
187 Fe, Mg, and K than fresh biotite (Dong et al., 1998; Murphy et al., 1998). This phase was
188 detected in the saprolite, but not in the fresh rock (Dong et al., 1998). Next, altered biotite
189 weathers to kaolinite in the saprolite either via epitaxial overgrowth of two layers of kaolinite
190 onto one layer of altered biotite or in a 1:1 ratio with the formation of an intermediate halloysite
191 layer (Dong et al., 1998; Murphy et al., 1998). Within the rindlet zone, plagioclase, hornblende,
192 and chlorite must weather completely because these minerals are not found in the saprolite
193 (Murphy et al., 1998; White et al., 1998; Turner et al., 2003). In the present paper we explore the
194 weathering reactions occurring within the rindlet zone and at all of the interfaces associated with
195 the rindlet zone: corestone-rindlet, rindlet-saprolite, and the multiple parallel rindlet-rindlet
196 interfaces.
197 In June 2003 and July 2004 we collected a suite of solid samples from the Rio Icacos
198 watershed including saprolite, corestone, and rindlets (Figures 1-2). Rindlets were sampled from
199 around a corestone exposed at a roadcut on Route 191 (Figure 3). The samples include the edge
200 of a corestone and a continuous 49 cm section of rindlets above the corestone, spanning the
201 entire rindlet sequence between corestone and saprolite. The corestone samples were collected

using a sledgehammer. The rindlet samples were carefully removed with a hammer and chisel, wrapped in plastic and packing tape, and labeled according to position and orientation. At the rindlet-saprolite interface, the rindlets are more friable, thinner, and lighter in color than the majority of the rindlet zone. Likewise, the saprolite just above the interface is slightly harder and darker in color than the bulk of the overlying saprolite. This 7 cm thick zone, consisting of four ~1 cm thick, highly weathered rindlets and roughly 3 cm of adjacent saprolite, we term the protosaprolite zone (Figure 2). The rindlet-saprolite interface runs through the protosaprolite zone. In this outcrop, we refer to the rindlet zone as the ~46 cm region containing all of the hard, cohesive rindlets between the corestone and the protosaprolite zone. Rindlet-bounding fractures anastamose and outer rindlets (further from the corestone) tend to split, complicating precise definition of a single rindlet. Therefore, samples bounded by parallel fractures along a chosen transect were defined as individual rindlets. Where the transect crossed anastamosing fractures or partially split rindlets, the sample was collected as a single piece and considered a single rindlet. Delicate saprolite and protosaprolite samples were coated with melted wax on at least one side before removal from the outcrop to preserve the structure and orientation.

## 2. ANALYTICAL METHODS

### 2.1. Sample Preparation and Analysis

Bulk densities of the rindlet samples were determined by coating samples with thin layers of rubber cement and immersing them in water to measure volume displacement. Bulk elemental analysis was performed on pulverized and sieved (150 μm) corestone, rindlet, and saprolite

222 samples. These analyses included major and minor elements by inductively coupled plasma
223 atomic emission spectrometry (ICP-AES) after lithium metaborate fusion digestion and FeO by
224 titration after a multi-acid digest (SGS Mineral Laboratories, Ontario, Canada). Sub-samples
225 from within individual rindlets were taken by careful grinding with a Dremel rotary tool
226 equipped with diamond points.
227 Minerals within thin sections prepared from each rindlet were identified using optical
228 microscopy and electron probe microanalysis (EPMA, Cameca SX-50). EPMA was also used to
229 measure the composition of crystals as a function of distance from the corestone and from rindlet
230 edges. Backscattered electron (BSE) images, mosaic maps of BSE images, and X-ray elemental
231 maps of the thin-sections were made on an FEI Quanta 400 SEM equipped with an energy
232 dispersive X-ray spectrometer (EDS). Modal analysis was performed on backscattered images
233 using XT-Docu software (v. 3.2, Soft-Imaging System GmbH, Münster, Germany) to point count
234 phases identified by the user based on the backscatter grayscale value and crystal morphology.
235 This technique has been used to measure porosity in weathering rinds (Dorn, 1995; Dixon et al.,
236 2006). To supplement microscopic phase identification in the highly weathered rindlets and in
237 the protosaprolite zone, X-ray diffraction (XRD) was performed on randomly oriented,
238 powdered samples on a Scintag X2 theta-theta goniometer with a copper target. A step scan was
239 used with a step size of 0.02° and 2 seconds per step.
240
241 **2.2. X-Ray Microprobe Imaging**
242 To look for incipient oxidation reactions within Fe(II)-containing phases in the corestone
243 that may be too small to identify with the above mentioned techniques, synchrotron micro-
244 fluorescence maps of mineral grains in thin sections were made at the Stanford Synchrotron

245 Radiation Laboratory (SSRL) on Beam Line 2.3. This technique permits identification of
246 microscale spatial variations in oxidation state and stoichiometry within single mineral grains.
247 Beam size on the sample was approximately 2 x 2 μm at full width half maximum using
248 Kirkpatrick-Baez (K-B) focusing optics (X-Radia). X-ray fluorescence data were recorded using
249 a single element Si Vortex detector (SSI). Monochromatic X-rays were selected using a water
250 cooled Si(220) phi=0 double crystal monochromator. The X-ray energy was calibrated to the first
251 inflection point of an Fe metal foil, E=7112 eV. Maps were collected at several incident energies
252 (7121, 7125, 7130 and 7142 eV) in continuous raster scanning mode in order to collect the
253 fluorescence at several distinguishing points within the Fe edge to determine Fe oxidation states
254 in the sample. Fluorescence maps were analyzed using the Microanalysis Toolkit (Webb, 2006).
255 Fe and K fluorescence counts were normalized to the measured intensity of the incident X-ray
256 beam ($I_0$). The proportion of Fe(II) and Fe(III) at each point in the map was determined by linear
257 least squares analysis based on the normalized fluorescence spectra of Fe(II) (0.2 M
258 $Fe(NH_4)_2(SO_4)_2$ solution) and Fe(III) ($Fe_2O_3$) standards. X-ray absorption near edge spectra
259 (XANES) were collected on the same beam line on spots of interest and microprobe data were
260 fitted to XANES spectra (Webb, 2006) to confirm phase identification.

261 **2.3. Mass Transfer Calculations**

262 In a weathering profile, the mass of an immobile element is, by definition, the same in
263 both the parent rock and the weathered material for some volume of material. However, the mass
264 fraction of the immobile element (e.g., g Ti $g^{-1}$ saprolite) in the weathered material will differ
265 from that in the parent if weathering processes have resulted in a change in density. By

comparing the mass fractions of mobile elements that of an immobile element the mass transfer (loss or gain of an element relative to the parent rock composition) can be documented (e.g., Brimhall and Dietrich, 1987; Anderson et al., 2002).

Mass transfer of individual elements relative to Ti was calculated for each rindlet and saprolite sample. Open-system mass transport is quantifiable in the present samples because the parent material is homogenous (Rio Blanco quartz diorite), of uniform age (Tertiary), and contains a relatively inert component (Ti) that is present in both the parent and product material (Chadwick et al., 1990). Because saprolite is isovolumetrically weathered rock, volumetric strain (change in volume as a result of stress), calculated on the basis of an assumed immobile element, should be near-zero. White et al. (1998) identified Ti as relatively immobile in the Puerto Rican saprolite relative to the bedrock. The relative immobility of Ti in the rindlet zone was confirmed by our calculations of very low volumetric strain with respect to Ti:

$$\varepsilon_{Ti,w} = \frac{\rho_p C_{Ti,p}}{\rho_w C_{Ti,w}} - 1 \qquad (1)$$

where $\varepsilon_{Ti,w}$ is the volumetric strain in the weathered ($w$) sample with respect to Ti, $\rho_w$ is the bulk density of the weathered material (rindlets), $\rho_p$ is bulk density of the parent ($p$) rock, $C_{Ti,w}$ is the mass fraction of Ti in the weathered material, and $C_{Ti,p}$ is the mass fraction of Ti in the parent rock. Ti occurs in the Rio Blanco quartz diorite parent rock as ilmenite and as a structural component of biotite that is not lost from the biotite lattice during weathering (Murphy et al., 1998). Thus we assume Ti to be immobile in order to estimate mass loss during weathering.

Mass transfer (gain or loss) of an element $j$ relative to the parent rock, represented by the mass transfer coefficient, $\tau_{Ti,j}$, can be calculated as:

$$\tau_{Ti,j} = \left( \frac{C_{j,w} C_{Ti,p}}{C_{j,p} C_{Ti,w}} \right) - 1, \quad (2)$$

Here, $C_{j,w}$ is the mass fraction of element *j* in the weathered material, and $C_{j,p}$ is the mass fraction of element *j* in the parent material. If $\tau_{Ti,j} = -1$, element *j* is entirely lost. If $\tau_{Ti,j} > 0$, a net gain of element *j* relative to the parent rock is indicated. The average of five analyses from a single corestone was used in the present calculations as the parent rock composition.

## 3. RESULTS

### 3.1. Porosity Development

Three types of cracks were observed in the system and will be referred to as macro-cracks, rindlet micro-cracks, and grain micro-cracks. The macro-cracks demarcate individual rindlets, run subparallel to the corestone-rindlet interface, and are easily observed in the outcrop (Figure 1). Rindlet micro-cracks, found within every rindlet we examined, are contained within individual rindlets, are not preferentially aligned, are not associated with any given mineral, and cut across multiple crystals of all phases indiscriminately. Density, length, and width of rindlet micro-cracks increase with distance away from the corestone, towards the saprolite (Figure 4). In the rindlets closest to the corestone, apertures of rindlet micro-cracks are < 10 μm wide and short (rarely extending across an entire 6 $mm^2$ SEM image). From about 20 cm above of the corestone (about halfway between the corestone and the saprolite) and beyond, rindlet micro-cracks that are 25-90 μm wide are common, with some as large as 250 μm wide (Figure 4c). By this point it

303 becomes difficult to image a 6 $mm^2$ area that does not contain rindlet micro-cracks that span the
304 image. Rindlet micro-cracks were not observed within the corestone.
305 Grain micro-cracks are associated with individual mineral grains and are typically
306 observed along cleavage planes or along grain boundaries. Grain micro-cracks are found
307 throughout all rindlets and are most noticeable within ~5 mm of the macro-cracks (along the
308 edges of every rindlet). Within the outer 9 or 10 mm of the corestone, occasional grain micro-
309 cracks are identifiable. No micro-cracks are recognized more than 10 mm into the corestone.
310 The bulk density decreases steadily across the rindlet zone, from 2.7 g $cm^{-3}$ for the
311 corestone to 1.8 g $cm^{-3}$ at the rindlet-saprolite interface (Figure 5a), and mirrors the increase in
312 porosity determined by point counting (Figure 5b). Porosity and low molecular weight pore-
313 filling precipitates were readily distinguished from the crystalline phases using EDS and SEM.
314 To limit variability in the point counts due to large rindlet micro-cracks and image resolution,
315 porosity and mineral phases in the majority of the rindlet zone were only counted on same-size
316 BSE images (~6 $mm^2$ areas) that did not contain rindlet micro-cracks that spanned the entire
317 image. However, the extensive network of micro-cracks made this impossible in the outermost.
318 For these samples, care was taken to avoid micro-cracks larger than ~60 μm wide.
319 Porosity in the corestone is extremely low (0.03 %) at approximately 36 mm below the
320 corestone-rindlet interface. Throughout the rindlet zone, non-crack porosity is dominated by
321 intra-crystal weathering of the hydrothermally altered calcic cores of zoned plagioclase crystals
322 (Figure 4b). Additional porosity is created by apatite crystals, which weather inward from the
323 edges, forming apatite-shaped pores (Figure 4d). Apatite crystals are mostly present as inclusions
324 within hornblende and biotite and less commonly within primary iron oxides. They are also

found adjacent to other primary minerals. With increasing distance from the corestone, apatite content decreases, while the abundance of apatite-shaped pores increase.

### 3.2. Chemical Mobility

Calculations of the mass transfer coefficient, $\tau_{Ti,j}$ (Equation 2), indicate the average order of cation mobility in the entire rindlet zone relative to the corestone: P > Ca ~Na > Fe(II) > K > Mn > Si ~Mg > Fe (total) > Al, which differs from what has been calculated for the saprolite: Na ≈ Ca > Mg > Si > K > Al > Fe (total) (White et al., 1998). The most notable difference is the lower mobility of Mg in the rindlet zone relative to the saprolite. These results suggest rapid weathering of plagioclase and apatite and slower weathering of Fe-silicates (all of which contain Mg) in the rindlet zone, relative to the saprolite where Mg is lost during the weathering of biotite (Murphy et al., 1998; White et al., 1998).

Mass transfer coefficients also reveal most of the rindlets to be only slightly depleted (or enriched) in most elements relative to the corestone. The largest bulk chemical differences relative to the corestone are found in the 7 cm thick protosaprolite zone (Table 1) indicating that the majority of the chemical weathering occurs over a very narrow zone. These chemical differences correlate with the relative degree of weathering observable in BSE images (Figure 4). These images reveal little difference between the rindlet samples and the corestone, with the exceptions of micro-cracks and plagioclase weathering in the rindlet samples. Within the protosaprolite zone, however, intense weathering is evident.

### 3.3. Mineralogy

346 The average mineralogical composition of the corestone determined by digital point
347 counting is given in Table 2 and is consistent with previous work on the Rio Blanco quartz
348 diorite bedrock (Seiders, 1971; Murphy et al., 1998; White et al., 1998; Turner et al., 2003).
349 Large (~200-1000 μm) plagioclase crystals with altered calcic cores are the most abundant
350 mineral, comprising ~50 vol %, followed by quartz at ~20 vol %. The altered plagioclase cores
351 are sericitized, typical of hydrothermal alteration. Fe-silicate phases include hornblende; biotite,
352 which is partially replaced by chlorite; and some other chlorite that does not have a biotite
353 morphology. The chlorite is typical of low-grade metamorphic or hydrothermal alteration.
354 Hornblende is the most abundant Fe-silicate phase, followed by biotite. No pyroxene was
355 observed and chlorite was relatively minor. Accessory minerals include primary Fe oxides with
356 ilmenite exsolution lamellae, sphene, apatite, and zircon. Mineral formulas for plagioclase and
357 the major Fe-silicate phases were determined by EPMA (Table 3).
358 With the exception of a slight increase in grain micro-cracking along rindlet edges, no
359 trends in mineralogy, chemistry, or porosity were recognized across individual rindlets (e.g.,
360 Figure 7), contradictory to the Turner et al. (2003) model of a series of multiple parallel
361 weathering fronts made up of individual rindlets. Also, with the notable exception of apatite and,
362 to a lesser extent, plagioclase, no distinct trend was noted in the distribution of mineral phases
363 throughout the intact rindlet zone. Throughout the most pristine half (~25 cm) of the rindlet
364 zone, precipitated weathering products are rare and mostly confined to plagioclase cores and
365 along some micro-cracks. Hornblende appears pristine throughout most of the rindlet zone.
366 Specifically, no reddening due to oxidation, no dissolution features, and no alteration to
367 secondary phases was observed. In fact, within the majority of the rindlet zone, plagioclase and
368 apatite inclusions commonly weather out leaving the surrounding hornblende essentially

369 unchanged and rindlet micro-cracks commonly cross-cut hornblende crystals without evidence of
370 chemical alteration or dissolution along the edges (Figure 4d).

371 In contrast, hornblende alteration is occasionally visible about 6 cm below the rindlet-
372 saprolite interface (in the last two intact rindlets below the protosaprolite zone). Here hornblende
373 begins to look more reddish and some zones of Fe enrichment can be detected although
374 dissolution features (e.g., etching) are not seen until the protosaprolite zone. In contrast to the
375 hornblende crystals in the corestone and in the rindlet zone, hornblende crystals in the
376 protosaprolite zone are significantly smaller and dramatically etched (Figure 6). Similar saw-
377 toothed etching along weathered hornblende cleavage planes has been reported by others (e.g.,
378 Berner and Schott, 1982; Anand and Gilkes, 1984; Velbel, 1989). Hornblende grains are
379 extremely difficult to find under SEM above the rindlet-saprolite interface, although XRD
380 patterns indicate that hornblende persists in the first 2 cm of the saprolite, but not beyond. EPMA
381 analyses (2-5 μm spot size) of >300 hornblende grains revealed no compositional changes as a
382 function of distance from the corestone (Figure 7).

383 As mentioned before, the rindlet-saprolite interface runs through the middle of the
384 protosaprolite zone (Figure 2). In the rindlet portion of the protosaprolite zone, primary mineral
385 grains are surrounded by abundant precipitated gibbsite with minor kaolinite identified by
386 elemental ratios measured by EDS and EPMA. Kaolinite becomes more abundant above the
387 saprolite-rindlet boundary. Boxwork replacement of primary iron oxide crystals by iron
388 (oxy)hydroxides (e.g., Nahon, 1986; Velbel, 1989; Delvigne, 1998) was observed only within the
389 protosaprolite zone. Quartz remains relatively pristine throughout the rindlet and the
390 protosaprolite zones (Figure 4). Specifically, no dissolution channels, no etch pits, and few grain
391 micro-cracks were observed in quartz grains.

Point counting of mineral phases in BSE images using image analysis software was difficult for individual Fe-silicate phases due to overlapping grayscale values, which are a function of the mean atomic number of the sample. Specifically, it was not possible to quantify the Fe-silicate minerals individually due to the partial hydrothermal, pseudomorphic replacement of biotite by chlorite and the similar chemistries (and hence similar average atomic numbers and grayscale values) of the chlorite, biotite, and hornblende in these samples. The volume percentages of these Fe-silicates (as a group) indicates that they are relatively constant over the rindlet zone, but decrease in abundance within the protosaprolite zone (Figure 8). Apatite, which was readily point-counted (~0.6 vol % in the corestone), is entirely lost within the rindlet zone.

Throughout the rindlet zone, the weathering of plagioclase from the calcic cores outward to the sodic rims (Figures 4b-c) and the oxidation of biotite are readily observed in thin sections under a petrographic microscope. Biotite grains appear more reddish in all of the rindlets than in the corestone, indicating oxidation. In the corestone, no evidence was found to indicate plagioclase weathering (distinct from preexisting hydrothermal alteration). Conversely, zones of oxidized iron within corestone biotite crystals were documented in X-ray microprobe images (Figure 9a) of biotite crystals 2.7 cm from the corestone-rindlet interface. Linear least square fitting of the Fe fluorescence counts at each energy measured at each point in the image map was performed to determine the Fe(II) and Fe(III) content of the sample (Figure 9). Fe(III)-K correlation plots show that areas of higher amounts of Fe(III) have lower K counts (Figure 10). Masking of these individual areas show that the center of the biotite grains have approximately constant ratios of Fe(III):K, while the altered regions are localized to the lower K/higher Fe(III) regions (Figure 11). XANES spectra of these zones were consistent with oxidized biotite and were not consistent with Fe(III)-(hydr)oxide phases nor hornblende (Figure 12). Oxidized biotite

415 could not be definitively distinguished from chlorite on the basis of XANES spectra alone, but
416 the two phases were easily differentiated by their relative ratios of K to total Fe, which are
417 relatively high in biotite, lower in the oxidized zones, and close to zero in chlorite. Thus the first
418 weathering reaction observed in this system is the oxidation of biotite within the corestone.

419 **4. DISCUSSION**

420 Based on our microscopic, spectroscopic, chemical, and diffraction data, the following
421 sequence of weathering reactions is proposed. First, within the corestone, diffusion of oxygen
422 into the fresh rock leads to oxidation of Fe(II) to Fe(III) within the biotite lattice, which loses $K^+$
423 ions from the interlayer to maintain charge balance:
424
425 $K_{0.89}(Fe^{2+}_{1.23}Fe^{3+}_{0.05}Mg_{1.19}Mn_{0.02}Ti_{0.18}Al_{0.16})(Si_{2.88}Al_{1.12})O_{10}(OH)_2$.
426 $+ 0.36\ H^+ + 0.09\ O_2 \rightarrow 0.18\ H_2O + 0.36\ K^+ +$
427 $K_{0.53}(Fe^{2+}_{0.87}Fe^{3+}_{0.41}Mg_{1.19}Mn_{0.02}Ti_{0.18}Al_{0.16})(Si_{2.88}Al_{1.12})O_{10}(OH)_2$. (3)
428
429 This reaction creates a form of biotite referred to as 'altered biotite' by Dong et al.
430 (1998), which is characterized by an expansion of the (001) d-spacing from 10 to 10.5 Å as well
431 as by the oxidation of lattice-bound Fe(II). In the low porosity corestone, this expansion builds
432 up elastic strain energy that leads to fracturing, forming a macro-crack demarcating an individual
433 rindlet. The macro-cracks act as conduits for fluids that penetrate into the rindlets along the
434 macro-crack boundaries to form grain micro-cracks, which tend to congregate along rindlet
435 boundaries and at the corestone-rindlet interface. Rindlet micro-cracks, which fracture multiple

mineral grains of multiple phases without following grain boundaries, also form after macro-cracking (i.e., they are not observed in the corestone), although the exact cause of these micro-cracks remains unknown. Regardless, rindlet micro-cracks permit penetration of fluids into the rindlet interiors, facilitating further biotite oxidation as well as plagioclase dissolution:

$$Na_{0.50}Ca_{0.48}K_{0.01}Al_{1.43}Si_{2.56}O_8 + 5.76\ H_2CO_3 + 2.24\ H_2O \rightarrow$$
$$+ 0.50\ Na^+ + 0.48\ Ca^{2+} + 0.01\ K^+ + 1.43\ Al^{3+} + 2.56\ H_4SiO_4 + 5.76\ HCO_3^- \quad (4)$$

As these reactions progress across the rindlet zone, some saprolitization reactions occur: complete loss of chlorite and oxidation of biotite to its saprolite composition. Within the protosaprolite zone, the final transformation of relatively hard, intact rindlets into soft, disaggregated saprolite takes place. This transformation is accomplished as the remaining plagioclase is lost, all of the hornblende dissolves to completion:

$$(Ca_{1.73}Na_{0.29}K_{0.06})(Mg_{2.64}Fe^{2+}_{1.95}Mn_{0.09}Ti_{0.12}Al_{0.37})(Si_{7.24}Al_{0.76})O_{22}(OH)_2$$
$$+ 16.56\ H_2CO_3 + 5.2\ H_2O \rightarrow 7.24\ H_4SiO_4 + 1.13\ Al^{3+} + 0.06\ K^+ + 0.29\ Na^+ + 1.73\ Ca^{2+}$$
$$+ 2.64\ Mg^{2+} + 1.95\ Fe^{2+} + 0.09\ Mn^{2+} + 0.12\ TiO_2 + 16.56\ HCO_3^- + 0.12\ O_2 \quad (5)$$

and goethite begins to form. Although hornblende dissolution is insignificant within the rindlet zone, the absence of hornblende in the saprolite indicates that complete dissolution must occur over the ~7 cm protosaprolite zone (Figure 6b). Although hornblende is also oxidized within the protosaprolite zone, this signal is eclipsed by the complete dissolution of the mineral.

458 Throughout the saprolite, altered biotite weathers to kaolinite (Murphy et al., 1998) and quartz
459 dissolves, developing etch pits (Schulz and White, 1999).

460 **4.1. Weathering Gradients and Reaction Stoichiometry**

461 In a steady state weathering profile, gradients in bulk chemical composition relative to
462 depth are generated by the weathering reactions taking place. Negative gradients (on plots of
463 depth vs. chemical composition) indicate a loss of a given element or mineral, while positive
464 slopes indicate an increase. Here we present solid state elemental weathering gradients ($b_s$ in m
465 kg mol$^{-1}$) following White (2002) from which we extract information about the various
466 weathering reactions occurring over the spheroidally weathering profile.
467 The mass fraction (e.g., g element g$^{-1}$ rock) of a mobile element that is not incorporated
468 into a secondary mineral after release from a weathering primary mineral, can be modeled as a
469 linear decrease from an initial mass fraction $C_0$ at depth $z_1$ to $C_w$ at a shallower depth $z_0$ (Figure
470 13). Here $C_0$ corresponds to the mass fraction of the element within the protolith (the corestone)
471 and $C_w$ is the mass fraction of the element in a weathered sample at some depth $z$. The value $C_w$
472 may differ from the measured value $C_{j,w}$ (Equation 2) due to changes in density during
473 weathering. These changes are estimated by normalizing the mass relative to an element that is
474 relatively inert to chemical weathering, here Ti:

$$C_w = C_{j,w}\left(\frac{C_{Ti,p}}{C_{Ti,w}}\right) \quad (\mathbf{6})$$

475 where $C_{Ti,p}$ (mol kg$^{-1}$) is the mass fraction of the assumed inert element (Ti) in the protolith and
476 $C_{Ti,w}$ is the mass fraction of Ti in the weathered material. This normalization is based on the same

477 principles as the calculation of the mass transfer coefficient (Equation 2) and can be easily
478 converted:

$$\tau_{Ti,j} = \frac{C_w}{C_{j,p}} - 1 \quad (7)$$

479 Values of $C_w$ with depth for several elements are shown in Figure 14 with linear fits.
480 Within the profile studied here, two discrete weathering gradients can be discerned for several
481 elements (Fe, K, Mg, and Mn): the first across the rindlet zone, the second through the
482 protosaprolite zone (Figure 2). Assuming a steady state profile, differences in gradient for a
483 single element in the protosaprolite versus in the rindlet zone indicate a change in the rate of
484 release of that element, which can signify a change in mineral weathering rates and/or a change
485 in the reactions taking place. For example, the weathering gradient in Fe(II) is significantly
486 shallower across the protosaprolite zone ($b_s$ = 0.088 m kg mol$^{-1}$) than in the rindlet zone ($b_s$ =
487 2.02 m kg mol$^{-1}$, Figure 14a) indicating a more rapid loss of Fe(II) in the protosaprolite and
488 potentially a different reaction. Because the weathering gradients in Fe(III) across the rindlet and
489 protosaprolite zones (Figure 14b) are reversed with respect to the gradients in Fe(II) (Figure
490 14a), it is clear that Fe(II) is lost via oxidation to Fe(III), rather than by removal from the system.
491 In a multi-mineralic system, multiple weathering reactions may occur simultaneously,
492 each contributing to the elemental weathering gradients in different proportions. The loss of Mg
493 (Figure 14c) in the rindlet and protosaprolite zones could result from the dissolution of biotite,
494 hornblende, or chlorite, or the oxidation of hornblende. The loss of K (Figure 14d) could be
495 caused by biotite oxidation or dissolution of biotite or hornblende; and the loss of Mn (Figure
496 14f) could indicate dissolution of hornblende or biotite. The loss of Fe(II) over the rindlet zone
497 could be caused by any of the following reactions: dissolution of hornblende, oxidation of Fe(II)

498 in hornblende, dissolution of biotite, oxidation of Fe(II) in biotite, dissolution of chlorite, or
499 oxidation of Fe(II) in chlorite. These reactions involve $Fe^{2+}$ as well as $K^+$ and/or $Mg^{2+}$. We can
500 represent these reactions by their stoichiometries with respect to these ions. The stoichiometry of
501 biotite oxidation is 1 mol $Fe^{2+}$ oxidized per mol $K^+$ lost and the stoichiometry of hornblende
502 oxidation is 2 mol $Fe^{2+}$ oxidized per mol $Mg^{2+}$ lost.

503 To estimate the relative importance of the different Fe-silicate weathering reactions
504 occurring within the rindlet zone, we set up and solve a system of equations describing the
505 weathering gradients for several elements (Fe(II), Mg, K, and Mn) as functions of the
506 stoichiometries of the possible reactions:

$$\frac{1}{b_{Fe(II)}} = \nu_{b,o}^{Fe(II)} M_{b,o} + \nu_{h,o}^{Fe(II)} M_{h,o} + \nu_{b,d}^{Fe(II)} M_{b,d} + \nu_{h,d}^{Fe(II)} M_{h,d} + \nu_{c,d}^{Fe(II)} M_{c,d} \quad (8)$$

$$\frac{1}{b_K} = \nu_{b,o}^{K} M_{b,o} + \nu_{b,d}^{K} M_{b,d} + \nu_{h,d}^{K} M_{h,d} \quad (9)$$

$$\frac{1}{b_{Mg}} = \nu_{h,o}^{Mg} M_{h,o} + \nu_{b,d}^{Mg} M_{b,d} + \nu_{h,d}^{Mg} M_{h,d} + \nu_{c,d}^{Mg} M_{c,d} \quad (10)$$

$$\frac{1}{b_{Mn}} = \nu_{b,d}^{Mn} M_{b,d} + \nu_{h,d}^{Mn} M_{h,d} \quad (11)$$

507 Here $b_s$ is a weathering gradient (m kg $mol^{-1}$) where $s$ = Fe(II), K, Mg, or Mn and $\nu_{i,j}^{x}$
508 represent the stoichiometric coefficients for $x$ = Fe(II), K, Mg, and Mn, and subscripts $i = b, h,$ or
509 $c$ indicating biotite, hornblende, chlorite, respectively, and $j = o$ or $d$ indicating oxidation or
510 dissolution, respectively. For example, $\nu_{b,o}^{Fe(II)}$ indicates the moles of Fe(II) "lost" per mol of
511 biotite oxidized. These values are listed in Table 4. $M$ indicates the quantity (mol $m^{-1}$ $kg^{-1}$) of
512 mineral ($b, h,$ or $c$) undergoing either oxidation or dissolution ($o$ or $d$) in the rindlet zone. We

513 reduce the unknowns from 5 to 4 by assuming that all chlorite is dissolved over the rindlet zone.
514 This is reasonable because chlorite – the least abundant Fe-silicate phase in the bedrock – is not
515 observed in the protosaprolite or saprolite. This assumption gives $M_{c,d}$ = 0.185 mol $m^{-1}$ $kg^{-1}$ of
516 chlorite dissolved. Solving the system of equations yields $M_{b,d}$ = -1.0 mol $m^{-1}$ $kg^{-1}$, $M_{h,d}$ = 0.39
517 mol $m^{-1}$ $kg^{-1}$, $M_{b,o}$ = 2.8 mol $m^{-1}$ $kg^{-1}$, $M_{h,o}$ = -0.01 mol $m^{-1}$ $kg^{-1}$. The negative values for biotite
518 dissolution ($M_{b,d}$) and hornblende oxidation ($M_{h,o}$) likey reflects the sequestration of Mg-within
519 secondary phases or loss of Mg during biotite oxidation, which was not considered here.
520 Vermiculite layers interstratified with altered biotite in the protosaprolite zone are one likely
521 candidate for a Mg sink. This intermediate phase, although detected by XRD and TEM in the
522 saprolite by Murphy et al. (1998) and Dong et al. (1998), were not modeled here because they
523 vary in composition and are a very small component of the total mineralogy. Despite this
524 simplification, these results clearly show that Fe(II) loss across the rindlet zone is dominated by
525 biotite oxidation. Optically, hornblende oxidation does not appear to be significant within the
526 rindlet zone. This conclusion is supported by these calculations and by EPMA results, which do
527 not indicate any loss of cations from hornblende as a function of distance across the rindlet zone
528 (Figure 7).

529 The stoichiometric coefficients for Fe and K during biotite oxidation, $\nu_{b,o}^{Fe(II)}$ and $\nu_{b,o}^{K}$,
530 represent an increase in ferric iron in the mineral formula of 26.3%: the observed difference in
531 oxidation between bedrock biotite and biotite in the deepest saprolite (Murphy et al., 1998). If we
532 assume 3.7% of the biotite iron in the corestone is ferric following Murphy et al. (1998), then
533 convert an additional 26.3% of the ferrous iron to ferric, removing the molar equivalent in K, the
534 resulting composition is consistent the measured biotite compositions (EPMA) in the
535 protosaprolite. These results are consistent with a model in which iron in biotite is oxidizing

536 across the rindlet zone and ejecting $K^+$ ions to compensate for the loss of electrons. These results
537 also indicate that biotite achieves the oxidation state of the saprolite biotite (Murphy et al., 1998)
538 within the rindlet zone.

539 When a chemical gradient can be assigned to a mineral weathering reaction, that gradient
540 can be thought of as the weathering front for that particular reaction. Thus the Na gradient in the
541 rindlet zone defines the plagioclase weathering front and the Fe(II) gradient through the rindlet
542 and protosaprolite zones define the biotite oxidation and hornblende dissolution fronts,
543 respectively. In the saprolite, the K gradient defines the biotite dissolution front (Buss, 2006).
544 Therefore, although the bedrock-saprolite interface (i.e., the rindlet zone) can be thought of as
545 the bedrock weathering front, the system contains individual mineral weathering fronts that
546 occur in different portions of the profile and at different rates (Figure 15).

547 **4.2. Quantification of mineral weathering rates**

548 Elemental weathering gradients as discussed above can also be used to calculate long-
549 term, average mineral reaction rates. Using the methodology of White (2002) we use the solid
550 state weathering gradients (Figures 13-14) to calculate weathering rates across the rindlet zone
551 for hornblende and plagioclase dissolution and biotite oxidation.

552 The solid-state reaction rate *R* for a given mineral in a weathering profile is calculated
553 from the elemental distribution in the profile using the following expression from White (2002):

$$R = 10^{-3} \frac{1}{\varphi \beta s} \frac{\omega}{b_s} \tag{12}$$

554 where $\varphi$ is the mass fraction of the mineral in the weathering material (g $g^{-1}$), $\beta$ is the
555 stoichiometric coefficient of the element in the mineral (mol $mol^{-1}$), $s$ is the specific surface area
556 of the mineral ($m^2$ $g^{-1}$), $b_s$ is the weathering gradient (m kg $mol^{-1}$), and ω is the weathering
557 advance rate (m $s^{-1}$). Here the weathering advance rate equals the total denudation rate.

558 **4.3. Biotite weathering**

559 In powder XRD analyses and TEM images, Murphy et al. (1998) and Dong et al. (1998)
560 both noted the presence of an altered biotite phase in the Rio Icacos saprolite having a d (001)
561 spacing of 10.5 Å (compared to the 10.0 Å typical of biotite); higher Al/Si and Fe(III)/Fe(II)
562 ratios; and lower total Fe, Mg, and K than fresh biotite. XRD patterns of these altered biotite
563 grains contain a (060) peak at 1.55 Å indicating a trioctahedral structure. A peak was not
564 observed at 14 Å, characteristic of vermiculite or chlorite (Murphy et al., 1998). Similarly, $Mg^{2+}$
565 saturation did not yield a 24 Å peak and the 10.5 Å peak did not shift after Mg-saturation, $Mg^{2+}$
566 saturation/ethylene glycol solvation, $K^+$ saturation, or $K^+$ saturation with heating to 110ºC
567 (Murphy et al., 1998), all traditional indicators of interstratified vermiculite (e.g., Malla and
568 Douglas, 1987; Sawhney, 1989). However, Murphy et al. (1998) identified several 14 Å layers in
569 biotite grains using TEM and interpreted the 10.5 Å d (001) peak and a co-existing 3.37 Å peak
570 as evidence for a randomly interstratified biotite/vermiculite phase (sometimes called
571 hydrobiotite) containing ~12% vermiculite. This interpretation was made based on Mérings
572 principles (summarized by Moore and Reynolds, 1997), which state that randomly interstratified
573 phases will produce reflections between the (001) peaks of the endmembers (e.g., 10.0 Å biotite
574 and 14 Å vermiculite) that are shifted relative to the proportion of the two endmembers in the

575 mixed structure. When Dong et al. (1998) measured altered biotite d (001) spacings with TEM
576 excluding the 14 Å layers, the 10.5 Å spacings were still observed. This result was taken as
577 evidence that the altered biotite is a separate phase, distinct from both fresh biotite and
578 interstratified vermiculite/biotite. Possible causes of the expansion from 10.0 to 10.5 Å were not
579 discussed by Dong et al. (1998).

580 The altered biotite phase was found in the saprolite but not in the bedrock, and was
581 therefore presumed to form at the bedrock-saprolite interface (Dong et al., 1998), in other words,
582 within the rindlet zone. Murphy et al. (1998) noted that biotite in the saprolite is oxidized relative
583 to biotite in the bedrock. Gradients in Fe(II) and K across the rindlet zone (Figures 14a and 14d)
584 indicate that biotite oxidation occurs there, consistent with the formation of an oxidized "altered
585 biotite" phase. However, we also documented zones of biotite oxidation coupled with K-
586 depletion in the bedrock corestone (Figure 11), apparently preceding dissolution reactions and
587 porosity development.

588 The expansion of biotite layers from 10.0 to 10.5 Å during oxidation is consistent with
589 the model proposed by Fletcher et al. (2006). The weathering gradient for Fe(II) through the
590 rindlet zone is consistent with the reaction profile calculated by Fletcher et al. (2006) (Figure
591 16). This result, coupled with evidence that biotite oxidation is the first weathering reaction that
592 occurs in the corestone, suggests that biotite oxidation to form altered biotite is most likely the
593 reaction that initiates spheroidal fracturing. Dilation of biotite has been proposed by several
594 researchers as a mechanism for fracturing granite (e.g., Eggler et al., 1969; Isherwood and Street,
595 1976; Bustin and Mathews, 1979; Dixon and Young, 1981). However, the expansion is typically
596 explained as caused by the formation of vermiculite layers or other clays during biotite
597 weathering (e.g., Eggler et al., 1969; Isherwood and Street, 1976). The relatively smaller

598 expansion that occurs during the oxidation of biotite may be a novel explanation for reaction-
599 induced fracturing in granitic rock.

600 A weathering rate for the oxidation of biotite in the rindlet zone can be determined using
601 Equation 12 and the weathering gradient of Fe(II) across the rindlet zone ($b_s$ = 2.02 m kg mol$^{-1}$)
602 and the average weathering advance rate, ω, of 43 m Ma$^{-1}$ (Brown et al., 1995). Other parameters
603 used are $\varphi$ = 0.095 g g$^{-1}$ (White et al., 1998); specific BET surface area for fresh biotite, $s$ = 0.1
604 m$^2$ g$^{-1}$ (Acker and Bricker, 1992); and $\beta$ = 0.36 mol Fe(II) mol$^{-1}$, which is the stoichiometric
605 coefficient of Fe(II) oxidation ($\nu_{b,o}^{Fe(II)}$, Table 4). The resulting rate of biotite oxidation within the
606 rindlet sequence is 8.2 x 10$^{-14}$ mol m$^{-2}$ s$^{-1}$, or log R = -13.1. By comparison, the rate of biotite
607 weathering to kaolinite within the saprolite is log R = -15 (Murphy et al., 1998).

608 **4.4. Plagioclase weathering**

609 Plagioclase weathering occurs steadily across the rindlet and protosaprolite zones, as
610 evidenced by the Na gradient (Figure 14e), and produces the porosity (void space within remnant
611 plagioclase rims observed in thin sections) that eventually causes the rindlets to disintegrate in
612 the protosaprolite zone. Equation 12 can again be used to calculate a plagioclase weathering rate
613 from the Na gradient ($b_s$ = 0.45 m kg mol$^{-1}$) and mineralogical parameters $\varphi$ = 0.564 g g$^{-1}$ (White
614 et al., 1998), $\beta$ = 0.5 mol Na mol$^{-1}$ (Table 3), and $s$ = 0.1 m$^2$ g$^{-1}$. This specific BET surface area is
615 an average value for fresh oligoclase or andesine of 300-600 μm grain size (Holdren and Speyer,
616 1987), which is within the range of plagioclase grain sizes in the corestone and rindlets (~200 –
617 1000 μm). The resulting rate of plagioclase weathering is 1.1 x 10$^{-13}$ mol m$^{-2}$ s$^{-1}$, or log R = -
618 13.0. This rate is faster than that reported by Turner et al. (2003) for rindlet system plagioclase

619 weathering (log R = -14.3 to -14.6). Although Turner et al. (2003) used a range of specific
620 surface areas (0.1 – 1.0 $m^2 g^{-1}$), our rates are still faster even using this range (log R = -13.0 to -
621 14.0). This apparent discrepancy may be a matter of scale. Turner et al. (2003) calculated
622 average plagioclase weathering rates using sections of rindlet sets exhibiting different degrees of
623 weathering from different rindlet sequences within the watershed. One would expect rindlet sets
624 of different orientations, overlying saprolite thicknesses, elevations, and proximity to surface
625 waters to have slightly different weathering rates. Consequently, a rate that incorporates data
626 from several different sample sets can be considered to be an average rate over a larger area. The
627 rate presented here considers a single sub-horizontal rindlet zone atop a corestone and is
628 therefore averaged over a smaller, more densely sampled scale.

629 **4.5. Hornblende Weathering**

630 Previous researchers who have studied the Rio Icacos weathering system have noted the
631 absence of hornblende in the saprolite (White et al., 1998; Turner et al., 2003). Hornblende is the
632 most abundant Fe-silicate in the bedrock, but the mechanism and location of hornblende
633 weathering has not been previously identified. Pseudomorphic replacement of hornblende by
634 clay minerals such as chlorite, chlorite-saponite, or saponite has been documented in soil and
635 saprolite (Wilson and Farmer, 1970; Anand and Gilkes, 1984), but no widespread evidence for
636 such phase changes was observed in the present samples. Similarly, dissolution of hornblende
637 and re-precipitation of iron (oxy)hydroxides, gibbsite, or kaolinite can occur in soil, saprolite,
638 and weathering rinds ( e.g., Velbel, 1989), but was not observed in the rindlet samples: i.e., we
639 observed no etching of the hornblende grains, no boxwork texture or precipitates associated with

640 the rindlet hornblende crystals. In fact, plagioclase and apatite inclusions within hornblende
641 crystals are commonly seen to weather leaving the surrounding hornblende visibly un-weathered
642 (Figure 4d). EPMA and EDS analyses confirm that the surrounding hornblende is not
643 measurably altered (Figure 7). These results suggest that hornblende dissolution and subsequent
644 precipitation of Fe(III) (oxy)hydroxides is not the reaction that produces the positive $\Delta V_{reaction}$
645 that initiates spheroidal fracturing as suggested by Fletcher et al. (2006).
646 In some systems, hornblende weathering can also be detected optically by color changes
647 from dark green to pale green due to loss of iron, or to brown-ish green, due to oxidation of iron
648 (Deer et al., 1962; Wilson and Farmer, 1970). Although hornblende crystals in the outermost
649 rindlets do appear to be slightly oxidized, overall, evidence for hornblende weathering within the
650 rindlet zone is scarce. Therefore, hornblende oxidation is also an unlikely candidate for the
651 reaction that causes the spheroidal fracturing. Although macro- and micro-cracks permit fluid
652 flow into the rindlet zone, total permeability remains low (Turner et al., 2003). Low permeability
653 coupled with high mineral/fluid ratios and increased solute (Al, Si, Na, Ca, Mg) concentrations
654 due to plagioclase and, to a lesser extent, chlorite dissolution are inferred to keep the pore fluid
655 within the rindlet zone saturated with respect to hornblende, preventing dissolution.
656 To estimate the dissolution rate of hornblende in the protosaprolite using Equation 12, we
657 consider the gradient in Fe(II) across the protosaprolite zone ($b_s$ = 0.088 m kg mol$^{-1}$, Table 4)
658 and mineralogical parameters $\varphi$ = 0.063 g g$^{-1}$ (White et al., 1998), $\beta$ = 1.95 mol Fe(II) mol$^{-1}$
659 (Table 4), and $s$ = 0.2 m$^2$ g$^{-1}$ (Brantley and Mellott, 2000). The resulting rate of hornblende
660 weathering is 6.3 x 10$^{-13}$ mol m$^{-2}$ s$^{-1}$ (log R = -12.2).
661 In a steady state profile, the 7 cm thickness of the protosaprolite zone represents a very
662 short time interval relative to the time required to develop the entire profile (about 3 m total

663 thickness at the sampled outcrop). Thus the complete loss of hornblende over the 7 cm
664 protosaprolite zone implies extremely rapid weathering, which is reflected by the calculated
665 hornblende weathering rate. This rate is faster than other published rates for hornblende
666 weathering in the field, but is within range of laboratory weathering rates (see compilations in
667 White and Brantley, 1995; Brantley, 2004). This similarity to laboratory rates is not so surprising
668 when we consider that the protosaprolite zone has high exposed mineral surface area, high
669 porosity, and high fluid flux. Typically mineral weathering rates estimated from field data are
670 calculated from watershed fluxes and are averaged over the time period of profile development.
671 In the present study, by densely sampling the weathering profile and calculating the hornblende
672 dissolution rate for only the ~7 cm thick zone where the reaction occurs, we obtain an *in-situ* rate
673 that is not "diluted" over the entire profile or watershed.
674 Microorganisms living at depth near the saprolite-bedrock interface may benefit from an
675 increase in availability of inorganic nutrients, Fe(II) in particular, which are released from the
676 bedrock during mineral weathering. The ferrous iron released from hornblende in the
677 protosaprolite zone provides substrate for iron-oxidizing bacteria (Buss et al., 2005). Because
678 most of the Fe(II) within biotite is oxidized *in-situ* rather than released, biotite does not
679 contribute significantly to the flux of Fe(II) available to deep saprolite microorganisms. Iron-
680 oxidizing bacteria fix $CO_2$, producing organic carbon to support heterotrophic organisms in the
681 ecosystem. Growth of lithoautotrophs such as iron-oxidizing bacteria in the Rio Icacos saprolite
682 are favored by substrate fluxes and are likely dominant at depth (Buss et al., 2005), contributing
683 to the formation of Fe(III)-(hydr)oxides in the saprolite. The flux of Fe(II) from hornblende
684 dissolution in the protosaprolite could support a maximum growth rate of $4.5 \times 10^{-5}$ mol C $m^{-3}$ $h^{-1}$
685 for iron-oxidizing bacteria, based on the model of Buss et al. (2005). Because these bacteria alter

686 the concentrations of Fe(II) and $O_2$, they may also affect the rate of spheroidal weathering.

687 **5. CONCLUSIONS**

688 The quartz diorite bedrock in the Rio Icacos watershed weathers spheroidally forming
689 corestones surrounded by zones of concentric, partially weathered rindlets overlain by saprolite.
690 This process produces two distinct weathering interfaces: 1) the bedrock-rindlet interface where
691 the disaggregation is initiated via spheroidal macro-cracking to form rindlets, and 2) the rindlet-
692 saprolite interface where the rindlets disintegrate into saprolite due to extensive micro-cracking
693 and the completion of plagioclase and hornblende weathering. Within the ~7 cm thick
694 protosaprolite zone, hornblende rapidly dissolves to completion at a rate of $6.3 \times 10^{-13}$ mol $m^{-2}$ $s^{-1}$
695 , providing the dominant flux of Fe(II) to the saprolite and the saprolite biota. However, within
696 the ~47 cm rindlet zone, hornblende weathering is insignificant, plagioclase dissolves at a rate of
697 $1.1 \times 10^{-13}$ mol $m^{-2}$ $s^{-1}$, and biotite is oxidized at a rate of $8.2 \times 10^{-14}$ mol $m^{-2} s^{-1}$. The oxidation of
698 biotite forms a K-deficient "altered biotite" with an expansion of the d (001) spacing from 10.0
699 to 10.5 Å. Oxidation of biotite was also identified within individual biotite grains in the bedrock
700 corestone by X-ray microprobe imaging and XANES as the earliest weathering reaction
701 documented in the bedrock. Expansion of biotite during oxidation within the corestone is
702 consistent with the reaction-driven spheroidal fracturing model of Fletcher et al. (2006) and is
703 likely the reaction responsible for initiating the spheroidal fracturing and thus the disaggregation
704 of intact bedrock. Oxidation of biotite begins when $O_2$ diffuses into the corestone, and thus the
705 weathering advance rate is dependent upon the concentration of $O_2$ in the pore water. This
706 concentration is expected to vary with regolith thickness, providing a positive feedback between

707 denudation and weathering advance rates. The ability to map oxidation states within individual
708 crystals using synchrotron-based techniques has proven invaluable for the observation of
709 incipient weathering reactions within "pristine" bedrock, facilitating identification of rate
710 limiting reactions in coupled processes such as spheroidal weathering.
711
712 *Acknowledgements.* We thank A.F. White and R.C. Fletcher for helpful discussions and field
713 support; D. Eggler and E. Merino for assistance with optical microscopy; M. Angelone and J.
714 Cantolina for analytical assistance; M. Rosario-Torres, J. Troester, and G. Hernandez for field
715 support; and S. Anderson and 3 anonymous reviewers for comments that helped improve the
716 manuscript. Funding provided by DOE grant no. DE-FG02-05ER15675, the Penn State
717 Biogeochemical Research Initiative for Education (BRIE) supported by NSF-IGERT grant no.
718 DGE-9972759, and the Penn State Center for Environmental Chemistry and Geochemistry. H.L.
719 Buss acknowledges fellowship support of the NSF Graduate Research Fellowship Program and
720 postdoctoral support from the National Academy of Sciences Research Associateship Program. S.L
721 Brantley acknowledges support from the Center for Environmental Kinetics Analysis supported by
722 NSF grant no. CHE-0431328. Portions of this research were carried out at the Stanford Synchrotron
723 Radiation Laboratory, a national user facility operated by Stanford University on behalf of the U.S.
724 Department of Energy, Office of Basic Energy Sciences. The SSRL Structural Molecular Biology
725 Program is supported by the Department of Energy, Office of Biological and Environmental
726 Research, and by the National Institutes of Health, National Center for Research Resources,
727 Biomedical Technology Program.

728 **References**


729 Acker, J. G. and Bricker, O. P., 1992. The influence of pH on biotite dissolution and alteration
730 kinetics at low temperature. *Geochim. Cosmochim. Acta* **56**, 3073-3092.
731 Anand, R. R. and Gilkes, R. J., 1984. Weathering of hornblende, plagioclase and chlorite in
732 meta-dolerite, Australia. *Geoderma* **34**, 261-280.
733 Anderson, S. P., Dietrich, W. E., and Brimhall, G. H., 2002. Weathering profiles, mass-balance
734 analysis, and rates of solute loss: Linkages between weathering and erosion in a small,
735 steep catchment. *Geological Society of America Bulletin* **114**, 1143-1158.
736 Begle, E. A., 1978. The Weathering of Granite, Llano Region Central Texas, The University of
737 Texas at Austin.
738 Berner, R. A. and Schott, J., 1982. Mechanism of pyroxene and amphibole weathering: II.
739 Observations of soil grains. *Amer. J. Sci.* **282**, 1214-1231.
740 Bisdom, E. B. A., 1967. The role of micro-crack systems in the spheroidal weathering of an
741 intrusive granite in Galicia (NW Spain). *Geologie en Mijnbouw* **46**, 333-340.
742 Boccheciamp, R. A., Rivera, W. F., Trigo, J. E., Brunet, J. E., Torres, E. O., McKinze, W. E.,
743 and Rivera, L. H., 1977. *Soil Survey of the Humacao Area of Eastern Puerto Rico*. USDA
744 Soil Conservation Service., Washington, D.C.
745 Brantley, S. L., 2004. Reaction kinetics of primary rock-forming minerals under ambient
746 conditions. In: Drever, J. I. (Ed.), *Surface and Groundwater, Weathering, and Soils*.
747 Elsevier, San Diego.
748 Brantley, S. L. and Mellott, N., 2000. Specific surface area and porosity of primary silicate
749 minerals. *Amer. Mineral.* **85**, 1767-1783.
750 Brimhall, G. and Dietrich, W. E., 1987. Constitutive mass balance relations between chemical
751 composition, volume, density, porosity, and strain in metasomatic hydrochemical
752 systems: results on weathering and pedogenisis. *Geochim. Cosmochim. Acta* **51**, 567-587.
753 Brown, E. T., Stallard, R., Larsen, M. C., Raisbeck, G. M., and Yiou, F., 1995. Denudation rates
754 determined from the accumulation of in situ-produced $^{10}$Be in the Luquillo Experimental
755 Forest, Puerto Rico. *Earth and Planetary Science Letters* **129**, 193-202.
756 Buss, H. L., 2006. Biogeochemical Weathering of Iron-Silicate Minerals. Ph.D. Thesis, The
757 Pennsylvania State University.
758 Buss, H. L., Bruns, M. A., Schultz, M. J., Moore, J., Mathur, C. F., and Brantley, S. L., 2005.
759 The coupling of biological iron cycling and mineral weathering during saprolite
760 formation, Luquillo Mountains, Puerto Rico. *Geobiology* **3**, 247-260.
761 Buss, H. L., Sak, P. B., White, A. F., and Brantley, S. L., 2004. Mineral dissolution at the
762 granite-saprolite interface. In: Wanty, R. B. and Seal, R. R. I. Eds.)*11th International*
763 *Symposium on Water-Rock Interaction*. Taylor and Francis, Saratoga Springs, NY.
764 Bustin, R. M. and Mathews, W. H., 1979. Selective weathering of granitic clasts. *Can. J. Earth*
765 *Sci.* **16**, 215-223.
766 Chadwick, O. A., Brimhall, G. H., and Hendricks, D. M., 1990. From black box to a grey box: a
767 mass balance interpretation of pedogenesis. *Geomorphology* **3**, 369-390.
768 Chatterjee, A. and Raymahashay, B. C., 1998. Spheroidal weathering of Deccan Basalt: a three-
769 mineral model. *Quarterly Journal of Engineering Geology* **31**, 175-179.

770 Deer, W. A., Howie, R. A., and Zussman, J., 1962. *Rock Forming Minerals Vol. 2: Chain*
771 *Silicates*. Longmans, London.
772 Delvigne, J. E., 1998. *Atlas of Micromorphology of Mineral Alteration and Weathering*.
773 Mineralogical Association of Canada, Ottawa.
774 Dixon, J. C., Campbell, S. W., Thorn, C. E., and Darmody, R. G., 2006. Incipient weathering
775 rind development on introduced machine-polished granite discs in an Arctic alpine
776 environment, northern Scandinavia. *Earth Surface Processes and Landforms* **31**, 111-
777 121.
778 Dixon, J. C. and Young, R. W., 1981. Character and origin of deep arenaceous weathering
779 mantles on the Bega Batholith, southeastern Australia. *Catena* **8**, 97-109.
780 Dong, H., Peacor, D. R., and Murphy, S. F., 1998. TEM study of progressive alteration of
781 igneous biotite to kaolinite throughout a weathered soil profile. *Geochim. Cosmochim.*
782 *Acta* **62**, 1881-1887.
783 Dorn, R., 1995. Digital processing of back-scatter electron imagery: a microscopic approach to
784 quantifying chemical weathering. *Geological Society of America Bulletin* **107**, 725-741.
785 Dosseto, A., Turner, S. P., and Chappell, J., Subm. The evolution of weathering profiles through
786 time: new insights from uranium-series isotopes. *Submitted to EPSL*.
787 Eggler, D. H., Larson, E. E., and Bradley, W. C., 1969. Granites, grusses, and the Sherman
788 erosion surface, southern Laramie Range, Colorado-Wyoming. *Amer. J. Sci.* **267**, 510-
789 522.
790 Farmin, R., 1937. Hypogene exfoliation in rock masses. *Journal of Geology* **45**, 625-635.
791 Ferry, J. M., 1984. Landforms of spheroidally weathered rock. In: Smiley, T. L., Nations, J. D.,
792 Pewe, T. L., and Schafer, J. P. Eds.), *Landscapes of Arizona*. University Press of
793 America, Lanham, MD.
794 Fletcher, R. C., Buss, H. L., and Brantley, S. L., 2006. A spheroidal weathering model coupling
795 porewater chemistry to soil thicknesses during steady-state denudation. *Earth and*
796 *Planetary Science Letters* **244**, 444-457.
797 Fritz, S. J. and Mohr, D. W., 1984. Chemical alteration in the micro weathering environment
798 within a spheroidally-weathered anorthosite boulder. *Geochimica Cosmochemica Acta*
799 **48**, 2527-2535.
800 Fritz, S. J. and Ragland, P. C., 1980. Weathering rinds developed on plutonic igneous rocks in
801 the North Carolina piedmont. *Amer. J. Sci.* **280**, 546-559.
802 Gilbert, G. K., 1904. Domes and dome structure of the High Sierra. *Geological Society of*
803 *America Bulletin* **15**, 29-36.
804 Heald, M. T., Hollingsworth, T. J., and Smith, R. M., 1979. Alteration of sandstone as revealed
805 by spheroidal weathering. *Journal of Sedimentary Petrology* **49**, 901-909.
806 Heimsath, A. M., Dietrich, W. E., Nishiizumi, K., and Finkel, R. C., 1999. Cosmogenic nuclides,
807 topography, and the spatial variation of soil depth. *Geomorphology* **27**, 151-172.
808 Holdren, G. R. and Speyer, P. M., 1987. Reaction rate-surface area relationships during the early
809 stages of weathering. II. Data on eight additional feldspars. *Geochemica Cosmochimica*
810 *Acta* **51**, 2311-2318.
811 Isherwood, D. and Street, A., 1976. Biotite-induced grussification of the Boulder Creek
812 Granodiorite, Boulder County, Colorado. *Geological Society of America Bulletin* **87**,
813 366-370.

814 Larsen, E. S., 1948. Batholith and associated rocks of Corona, Elsinore and San Luis Rey
815 quadrangles, southern California. *Geological Society of America Memoir* **29**, 114-119.
816 Le Pera, E. and Sorriso-Valvo, M., 2000. Weathering and morphogenesis in a mediterranean
817 climate, Calabria, Italy. *Geomorphology* **43**, 251-270.
818 Linton, D. L., 1955. The problem of tors. *Geographical Journal* **121**, 470-487.
819 Malla, P. B. and Douglas, L. A., 1987. Identification of expanding layer silicates: Charge density
820 vs. expansion properties. In: van Olphen, H. e. a. (Ed.),*Proc. Int. Clay Conf.* Clay
821 Minerals Society.
822 Mignon, P. and Thomas, M. F., 2002. Grus weathering mantles - problems of interpretation.
823 *CATENA* **49**, 5-24.
824 Moore, D. M. and Reynolds, R. C., 1997. *X-Ray Diffraction and the Identification and Analysis*
825 *of Clay Minerals*. Oxford University Press, New York.
826 Murphy, S. F., Brantley, S. L., Blum, A. E., White, A. F., and Dong, H., 1998. Chemical
827 weathering in a tropical watershed, Luquillo Mountains, Puerto Rico; II. Rate and
828 mechanism of biotite weathering. *Geochim. Cosmochim. Acta* **62**, 227-243.
829 Nahon, D. B., 1986. Evolution of iron crusts in tropical landscapes. In: Coleman, S. M. and
830 Dethier, D. P. Eds.), *Rates of Chemical Weathering of Rocks and Minerals*.
831 Ollier, C. D., 1967. Spheroidal weathering, exfoliation and constant volume alteration. *Zeitschrift*
832 *fuer Geomorphologie* **11**, 103-108.
833 Ollier, C. D., 1971. Causes of spheroidal weathering. *Earth-Science Reviews* **7**, 127-141.
834 Ollier, C. D., 1988. Deep weathering, groundwater and climate. *Geografiska Annaler., Series A,*
835 *Phys. Geog.* **70**, 285-290.
836 Pavich, M. J., 1989. Regolith residence time and the concept of surface age of the Piedmont
837 peneplain. *Geomorphology* **2**, 181-196.
838 Riebe, C. S., Kirchner, J. W., and Finkel, R. C., 2003. Long-term rates of chemical weathering
839 and physical erosion from cosmogenic nuclides and geochemical mass balance. *Geochim.*
840 *Cosmochim. Acta* **67**, 4411-4427.
841 Romani, J. R. V. and Twidale, C. R., 1998. *Formas y paisajes graniticos. Forms and granitic*
842 *landscapes*. Universidade da Coruna, Coruna, Spain.
843 Sawhney, B. L., 1989. Interstratification in layer silicates. In: Dixon, J. B. and Weed, S. B. Eds.),
844 *Minerals in Soil Environments*. Soil Sci. Soc. Amer.
845 Scarciglia, F., Le Pera, E., and Critelli, S., 2005. Weathering and pedogensis in the Sila Grande
846 Massif (Calabria, South Italy): From field scale to micromorphology. *Catena* **61**, 1-29.
847 Schattner, I., . 1961. Weathering phenomena in the crystalline of the Sinai in the light of current
848 notions. *Bulletin of the Research Council of Israel, Section G: Geo-Sciences* **10G**, 247-
849 266.
850 Schulz, M. S. and White, A. F., 1999. Chemical weathering in a tropical watershed, Luquillo
851 Mountains, Puerto Rico; III. Quartz dissolution rates. *Geochim. Cosmochim. Acta* **63**,
852 337-350.
853 Seiders, V. M., 1971. Geologic map of the El Yunque quadrangle, Puerto Rico. U.S. Geological
854 Survey.
855 Sequeira Braga, M. A., Paquet, H., and Begonha, A., 2002. Weathering of granites in a temperate
856 climated (NW Portugal): granitic saprolites and arenization. *CATENA* **49**, 41-56.
857 Simpson, D. R., 1964. Exfoliation of the Upper Pocohontas sandstone, Mercer County, West
858 Virginia. *Amer. J. Sci.* **242**, 545-551.

859 Thomas, M. F., 1974. Granite landforms: a review of some recurrent problems of interpretation,
860 *Problems in Geomorphology: papers in honour of David L. Linton*. Institute of British
861 Geography, London.
862 Turner, B. F., Stallard, R. F., and Brantley, S. L., 2003. Investigation of in situ weathering of
863 quartz diorite bedrock in the Rio Icacos basin, Luquillo Experimental Forest, Puerto
864 Rico. *Chem. Geol.* **202**, 313-341.
865 USDA NCRS, 2002. Soil Survey of Caribbean National Forest and Luquillo Experimental
866 Forest, Commonwealth of Puerto Rico. USDA, Natural Resources Conservation Service,
867 Washington D.C.
868 Velbel, M. A., 1989. Weathering of Hornblende to Ferruginous Products by a Dissolution-
869 Reprecipitation Mechanism: Petrography and Stoichiometry. *Clays and Clay Minerals*
870 **37**, 515 - 524.
871 von Blanckenburg, F., Hewawasam, T., and Kubik, P. W., 2004. Cosmogenic nuclide evidence
872 for low weathering and denudation in the wet, tropical highlands of Sri Lanka. *Journal of*
873 *Geophysical Research* **109**, F03008.
874 Webb, S. M., 2006. SMAK: Sam's Microprobe Analysis Kit, V.0.25. Stanford Synchrotron
875 Radiation Laboratory.
876 White, A. F., 2002. Determining mineral weathering rates based on solid and soute weathering
877 gradients and velocities: application to biotite weathering in saprolites. *Chem. Geol.* **190**,
878 69-89.
879 White, A. F., Blum, A. E., Schulz, M. S., Vivit, D. V., Stonestrom, D. A., Larsen, M., Murphy,
880 S. F., and Eberl, D., 1998. Chemical weathering in a tropical watershed, Luquillo
881 Mountains, Puerto Rico: I. Long-term versus short-term weathering fluxes. *Geochim.*
882 *Cosmochim. Acta* **62**, 209-226.
883 White, A. F. and Brantley, S. L., 1995. Chemical weathering rates of silicate minerals: An
884 overview. In: White, A. F. and Brantley, S. L. Eds.), *Chemical Weathering Rates of*
885 *Silicate Minerals*. Mineralogical Society of America, Washington, D.C.
886 Wilson, M. J. and Farmer, V. C., 1970. A study of weathering in a soil derived from a biotite-
887 hornblende rock, II. The weathering of hornblende. *Clay Minerals* **8**, 435-444.
888

889 **Figure Captions**

890 **Figure 1. a)** Photograph of the primary sampling site along a roadcut on Route 191 (See map,
891 Figure 3). Here the ~1 m diameter corestone is surrounded by ~50 cm zone of rindlets and ~2 m
892 of saprolite. **b)** From Buss et al. (2004), close up photograph of the top of the corestone pictured
893 in a). The sub-horizontal rindlet sequence pictured was sampled in the present study.

894 **Figure 2.** Simplified diagram of the weathering profile in the Rio Icacos watershed. The quartz
895 diorite bedrock is rounded into corestones, which fracture concentrically forming a ~0.2-2 m
896 thick rindlet zone, overlain by 2-8 m of saprolite and 0.5-1 m of soil. The area immediately
897 surrounding the rindlet-saprolite interface is here called the "protosaprolite zone".

898 **Figure 3.** Maps of the field area. A star indicates location of the sampled road cut.

899 **Figure 4.** Backscattered electron (BSE) images of thin sections. **a)** Large zoned plagioclase
900 crystals dominate the un-fractured, apparently un-weathered corestone. **b)** In a rindlet ~8 cm
901 above the corestone-rindlet interface, occasional zoned plagioclase crystals partially dissolve and
902 form secondary precipitates within the interior of the crystals (shown with the thick black arrow),
903 quartz crystals are pristine, and partially chloritized biotite grains show no signs of dissolution or
904 alteration in BSE images. **c)** A rindlet sampled from ~20 cm above the corestone is typical of
905 most rindlets: all rindlets have rindlet micro-cracks (an example is shown with a white arrow)
906 that cut across multiple crystals while most hornblende crystals remain visibly un-altered
907 throughout the majority of the rindlet zone. **d)** In the last intact rindlet below the protosaprolite
908 zone, ~47 cm above the corestone-rindlet interface, chlorite is highly weathered, and hornblende,
909 although cracked, shows no obvious dissolution features. The arrow points to a round hole within
910 the hornblende where an apatite inclusion is believed to have dissolved without affecting the
911 adjoining hornblende (sub-spheroidal apatite inclusions are commonly observed in the unaltered

corestone). Note the difference in scale of this image. **e)** In the protosaprolite zone, ~2 cm below the rindlet-saprolite interface, plagioclase crystals are highly weathered and hornblende crystals show the first signs of dissolution. Quartz remains visibly un-altered throughout the rindlet and protosaprolite zones. **f)** In the protosaprolite zone, ~1 cm below the rindlet-saprolite interface, the plagioclase is almost entirely lost, much of the pore space created by dissolution of primary minerals is filled with gibbsite, and to a lesser extent, kaolinite. Here hornblende crystals are significantly smaller than they are in the corestone.

**Figure 5. a)** Individual rindlets show a steady decrease in bulk density as a function of distance from the corestone. **b)** Volume percent open porosity and total porosity (including low molecular weight secondary precipitates such as gibbsite filling pore spaces) determined by point counting using XT Docu software on backscattered electron images.

**Figure 6. a)** Backscattered electron images of the corestone reveal pristine hornblende crystals. **b)** Hornblende crystals in the protosaprolite zone contain dissolution features along cleavage planes and clumps of gibbsite and some kaolinite surround the crystals.

**Figure 7.** Fe/Si and Mg/Si ratios of hornblende crystal grains measured by EPMA as a function of distance from the corestone reveal no change in composition across the rindlet zone or across individual rindlets. The negative values on the y axis refer to samples within the corestone.

**Figure 8.** Volume percent composition of Fe-silicates (hornblende + biotite + chlorite) and of plagioclase with distance from the corestone. Modal analysis was performed by point counting using XT Docu software on backscattered electron images.

**Figure 9.** X-ray microprobe fluorescence maps showing **a)** Fe(III) and **b)** Fe(II) content in a biotite crystal within the corestone, 2.7 cm from the corestone-rindlet interface. The color scale runs from blue to red indicating least to most Fe(III) or Fe(II).

**Figure 10.** A plot of K versus Fe(III) fluorescence counts for the biotite grain shown in Figure 9 shows that areas of higher Fe(III) have lower K. The linear trend of points from the origin to the cluster of points indicating the biotite grain represents a constant ratio in Fe(III):K that is due to thinning along the edges of the biotite crystal. Note that the Fe(III):K ratios in the altered biotite region deviate significantly from the trend in Fe(III):K ratios along the crystal edges and thus cannot be attributed simply to variations in thickness.

**Figure 11.** X-ray microprobe fluorescence maps showing Fe(III) and K content of the biotite grain and altered biotite zones indicated in Figure 10. **a)** Fe(III) and **b)** K content in the bulk biotite crystal. **c)** Fe(III) and **d)** K content of the altered biotite zones. The color scale runs from blue to red indicating least to most Fe(III) or K.

**Figure 12.** X-ray absorption near edge spectra (XANES) of fresh and oxidized zones of a single biotite grain within a corestone thin section compared to XANES of mineral standards.

**Figure 13.** Schematic diagram (after White, 2002) depicting the distributions of a mobile element in a weathering profile.

**Figure 14.** Weathering gradients ($b_s$) for **a)** Fe(II), **b)** Fe(III) **c)** Mg, **d)** K, **e)** Na, and **f)** Mn, reveal two distinct trends for most elements: one through the rindlet zone, and one through the protosaprolite zone. Enrichments relative to the parent values seen as positive excursions at the protosaprolite zone were not included in the linear fits. These excursions are thought to be related to the horizontality of the particular rindlet sequence studied combined with the difference in permeability between the saprolite and the rindlet zone. This possibility should be further examined by analyzing sub-vertical rindlet sets from the sides of the corestones. For zones that were sub-sampled more intensively (protosaprolite, the corestone, and the first 3 rindlets), subsamples from single rindlets were averaged together.

**Figure 15.** Semi-schematic diagram indicating the location and gradient of the individual mineral weathering fronts in a generalized profile for the Rio Icacos watershed. $\tau_{Ti,\,j}$ is the mass transfer coefficient (Equation 2) where *j* = Na (plagioclase dissolution), Fe(II) (biotite oxidation or hornblende dissolution), or K (biotite dissolution). Dotted portions of the lines are extensions of the calculated values. Distance is set to zero at the rindlet-saprolite interface with positive values into the rindlet zone and negative values into the saprolite. The thin dashed line indicates the corestone-rindlet boundary. The biotite dissolution front was calculated from K data from Buss (2006) for a ridgetop saprolite profile near the roadcut studied here. However, this front should be considered approximate because Ti is a structural component of the biotite as well as the normalizing element. The plagioclase, hornblende, and biotite oxidation fronts were calculated from data collected on the roadcut samples in the present study.

**Figure 16.** Fletcher et al. (2006) modeled the oxidation of Fe(II) (as FeO for simplicity) in the corestone hornblende to produce an Fe(III) precipitate, which occurs with an increase in $\Delta V$, causing elastic strain energy to build up until the corestone fractures to produce a rindlet. The fraction of total Fe(II) that has reacted calculated by Fletcher et al. (2006) is shown here as a continuous line with steps representing the formation of rindlet-defining macro-cracks. Here we compare the profile calculated by the numerical model to the biotite oxidation gradient (the Fe(II) gradient across the rindlet zone, see Figure 14a), represented as $\tau_{Ti,Fe(II)}$ normalized to the 0-1 scale, where 0 = the saprolite-rindlet interface and 1 = the corestone-rindlet interface. Similar to the numerical model, biotite oxidation begins near the corestone with a large loss of Fe(II), followed by a leveling off near the saprolite.

Table 1: Mass transfer ($\tau_{Ti,j}$) of elements across the rindlet and protosaprolite zones

| Distance[a] | Al | Ca | Fe[b] | K | Mg | Mn | Na | P | Si | Fe(II) |
|---|---|---|---|---|---|---|---|---|---|---|
| Rindlet Zone | | | | | | | | | | |
| 0.00 | 0.03 | 0.02 | -0.02 | 0.09 | -0.02 | -0.04 | 0.03 | -0.05 | 0.01 | -0.01 |
| 0.70 | -0.01 | 0.05 | -0.05 | -0.38 | 0.05 | 0.02 | -0.05 | -0.17 | 0.08 | -0.13 |
| 5.50 | 0.79 | 0.58 | 0.02 | 0.68 | 0.17 | 0.04 | 0.88 | 0.05 | 0.59 | -0.09 |
| 9.00 | 0.04 | -0.01 | 0.02 | -0.02 | 0.06 | 0.07 | -0.02 | -0.01 | 0.06 | -0.03 |
| 14.50 | -0.07 | -0.23 | -0.03 | -0.19 | -0.11 | -0.05 | -0.14 | -0.15 | -0.05 | -0.23 |
| 21.50 | -0.03 | -0.23 | 0.02 | -0.13 | -0.05 | 0.02 | -0.15 | -0.21 | -0.03 | -0.21 |
| 30.00 | -0.36 | -0.55 | -0.05 | -0.20 | -0.10 | -0.12 | -0.53 | -0.64 | -0.29 | -0.30 |
| 39.00 | -0.36 | -0.58 | -0.11 | -0.25 | -0.12 | -0.16 | -0.57 | -0.44 | -0.38 | -0.33 |
| 45.00 | -0.30 | -0.57 | -0.16 | -0.16 | -0.10 | -0.18 | -0.55 | -0.37 | -0.37 | -0.36 |
| 47.35 | -0.08 | -0.08 | 0.02 | -0.24 | 0.24 | 0.18 | -0.15 | -0.35 | -0.01 | -0.02 |
| 47.95 | 0.10 | -0.15 | -0.06 | -0.13 | 0.02 | 0.01 | -0.05 | -0.39 | 0.04 | -0.19 |
| 48.00 | -0.11 | -0.39 | -0.03 | -0.17 | 0.04 | 0.02 | -0.38 | -0.37 | -0.20 | -0.24 |
| Protosaprolite | | | | | | | | | | |
| 48.45 | 0.44 | -0.19 | -0.02 | -0.21 | 0.07 | 0.00 | -0.05 | -0.41 | 0.11 | -0.14 |
| 48.75 | -0.09 | -0.74 | -0.12 | -0.29 | -0.09 | -0.20 | -0.75 | -0.82 | -0.44 | -0.39 |
| 49.40 | -0.48 | -0.81 | -0.07 | -0.48 | -0.20 | -0.29 | -0.87 | -0.90 | -0.47 | -0.41 |
| 50.20 | -0.40 | -0.88 | -0.16 | -0.60 | -0.38 | -0.45 | -0.94 | -0.95 | -0.50 | -0.57 |
| 51.00 | -0.23 | -0.90 | -0.16 | -0.70 | -0.49 | -0.52 | -0.94 | -0.95 | -0.42 | -0.65 |
| 52.00 | 2.13 | -0.98 | 0.33 | -0.85 | -0.75 | -0.36 | -0.96 | -1.00 | 0.35 | -0.89 |

[a] Distance in cm from the corestone-rindlet interface

[b] Fe is total iron.

Table 2: Average mineralogical composition[a] of the corestone

| Phase | Volume % |
|---|---|
| Porosity | 0.03 |
| Filled porosity[b] | 0.88 |
| Quartz | 19.9 |
| Plagioclase | 49.3 |
| Fe-silicates | 24.0 |
| Fe, Ti Oxides | 2.5 |
| Apatite | 0.62 |

[a] Volume % composition determined by point counting backscattered electron images of thin sections using image analysis software.

[b] Filled porosity is very fine-grained low molecular weight material found associated with cracks or pore space. In the corestone this material is dominantly pre-exisitng hydrothermal alteration products rather than weathering products.

Table 3: Mineral formulas measured by electron microprobe

| Mineral | Formula | Sample |
|---|---|---|
| Hornblende | $(Ca_{1.73}Na_{0.29}K_{0.06})(Mg_{2.64}Fe^{2+}_{1.95}Mn_{0.09}Ti_{0.12}Al_{0.37})(Si_{7.24}Al_{0.76})O_{22}(OH)_2$ | Corestone |
| Hornblende | $(Ca_{1.57}Na_{0.26}K_{0.06})(Mg_{2.66}Fe^{2+}_{1.91}Mn_{0.10}Ti_{0.10}Al_{0.47})(Si_{7.39}Al_{0.61})O_{22}(OH)_2$ | Middle rindlet[a] |
| Hornblende | $(Ca_{1.76}Na_{0.29}K_{0.07})(Mg_{2.66}Fe^{2+}_{1.99}Mn_{0.09}Ti_{0.11}Al_{0.33})(Si_{7.21}Al_{0.79})O_{22}(OH)_2$ | Protosaprolite |
| Biotite | $K_{0.89}(Fe^{2+}_{1.23}Fe^{3+}_{0.05}Mg_{1.19}Mn_{0.02}Ti_{0.18}Al_{0.16})(Si_{2.88}Al_{1.12})O_{10}(OH)_2$ | Corestone[b] |
| Biotite | $K_{0.73}(Fe^{2+}_{1.01}Fe^{3+}_{0.15}Mg_{1.16}Mn_{0.02}Ti_{0.18}Al_{0.28})(Si_{2.88}Al_{1.12})O_{10}(OH)_2$ | Middle rindlet |
| Biotite | $K_{0.33}(Fe^{2+}_{0.87}Fe^{3+}_{0.37}Mg_{1.06}Mn_{0.014}Ti_{0.18}Al_{0.35})(Si_{2.87}Al_{1.13})O_{10}(OH)_2$ | Protosaprolite |
| Chlorite[c] | $(Mg_{3.32}Fe^{2+}_{0.29}Fe^{3+}_{1.00}Al_{1.39})(Si_{1.61}Al_{2.39})O_{10}(OH)_8$ | Corestone |
| Plagioclase | $Na_{0.50}Ca_{0.48}K_{0.01}Al_{1.43}Si_{2.56}O_8$ | Corestone |

[a] The middle rindlet is located ~24 cm above the corestone and ~24 cm below the protosaprolite.

[b] Biotite formulas were calculated assuming that of the total Fe, 3.7% is Fe(III) for the corestone (Murphy et al., 1998), 13% for the middle rindlet, and 30% for the protosaprolite.

[c] After Turner et al. (2003).

Table 4: List of variables for Equations 8-11.

| | | | |
|---|---|---|---|
| $\nu_{b,o}^{Fe(II)}$ | 0.36 | mol mol$^{-1}$ | mol Fe(II) lost during biotite oxidation |
| $\nu_{h,o}^{Fe(II)}$ | 1.95 | mol mol$^{-1}$ | mol Fe(II) lost during hornblende oxidation |
| $\nu_{b,d}^{Fe(II)}$ | 1.23 | mol mol$^{-1}$ | mol Fe(II) lost during biotite dissolution |
| $\nu_{h,d}^{Fe(II)}$ | 1.95 | mol mol$^{-1}$ | mol Fe(II) lost during hornblende dissolution |
| $\nu_{c,d}^{Fe(II)}$ | 0.29[a] | mol mol$^{-1}$ | mol Fe(II) lost during chlorite dissolution |
| $\nu_{b,o}^{K}$ | 0.36 | mol mol$^{-1}$ | mol K lost during biotite oxidation |
| $\nu_{b,d}^{K}$ | 0.88 | mol mol$^{-1}$ | mol K lost during biotite dissolution |
| $\nu_{h,d}^{K}$ | 0.06 | mol mol$^{-1}$ | mol K lost during hornblende dissolution |
| $\nu_{h,o}^{Mg}$ | 0.973 | mol mol$^{-1}$ | mol Mg lost during hornblende oxidation |
| $\nu_{b,d}^{Mg}$ | 1.19 | mol mol$^{-1}$ | mol Mg lost during biotite dissolution |
| $\nu_{h,d}^{Mg}$ | 2.637 | mol mol$^{-1}$ | mol Mg lost during hornblende dissolution |
| $\nu_{c,d}^{Mg}$ | 3.32[a] | mol mol$^{-1}$ | mol Mg lost during chlorite dissolution |
| $\nu_{b,d}^{Mn}$ | 0.02 | mol mol$^{-1}$ | mol Mn lost during biotite dissolution |
| $\nu_{h,d}^{Mn}$ | 0.09 | mol mol$^{-1}$ | mol Mn lost during hornblende dissolution |
| $M_{b,o}$ | 2.81 | mol m$^{-1}$ kg$^{-1}$ | mol biotite oxidized per unit rock |
| $M_{h,o}$ | -0.01 | mol m$^{-1}$ kg$^{-1}$ | mol hornblende oxidized per unit rock |
| $M_{b,d}$ | -1.05 | mol m$^{-1}$ kg$^{-1}$ | mol biotite dissolved per unit rock |
| $M_{h,d}$ | 0.39 | mol m$^{-1}$ kg$^{-1}$ | mol hornblende dissolved per unit rock |
| $M_{c,d}$ | 0.185 | mol m$^{-1}$ kg$^{-1}$ | mol chlorite dissolved per unit rock |
| $b_{Fe(II)}$ | 2.02 | m kg mol$^{-1}$ | Fe(II) weathering gradient |
| $b_K$ | 8.92 | m kg mol$^{-1}$ | K weathering gradient |
| $b_{Mg}$ | 2.71 | m kg mol$^{-1}$ | Mg weathering gradient |
| $b_{Mn}$ | 72.3 | m kg mol$^{-1}$ | Mn weathering gradient |

[a]Chlorite variables determined from formula of Turner et al., 2003.

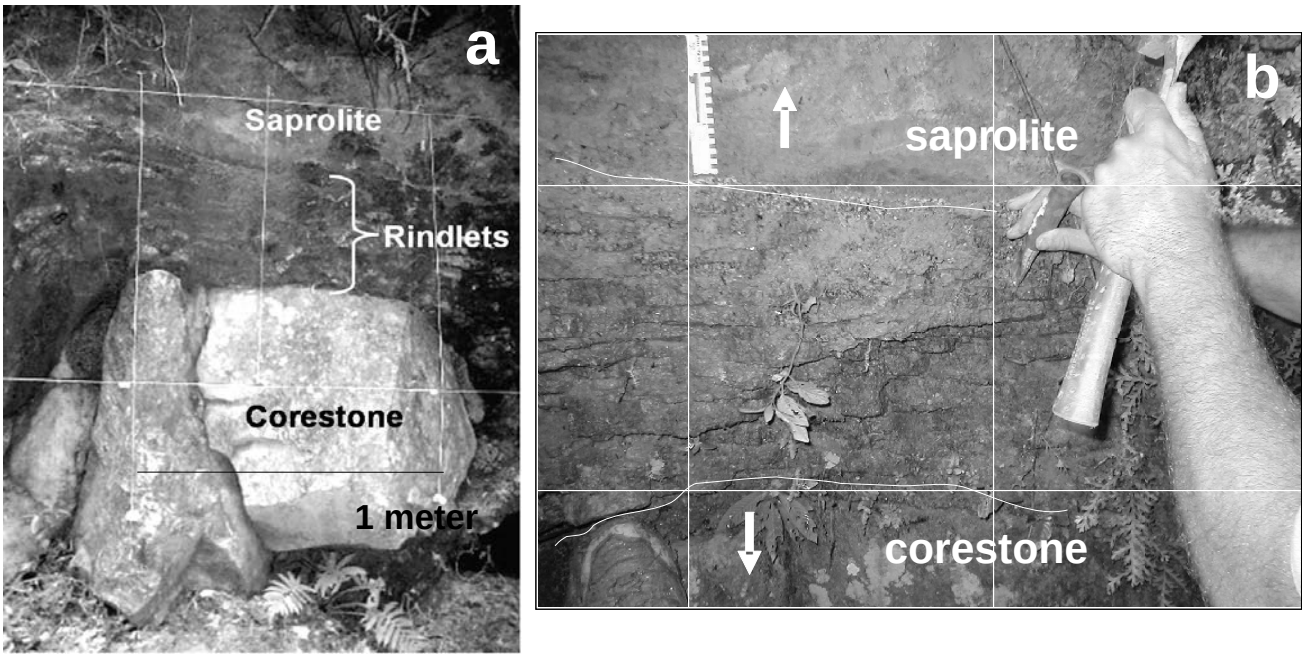
a
Saprolite
Rindlets
Corestone
1 meter
b
saprolite
corestone

Figure 1

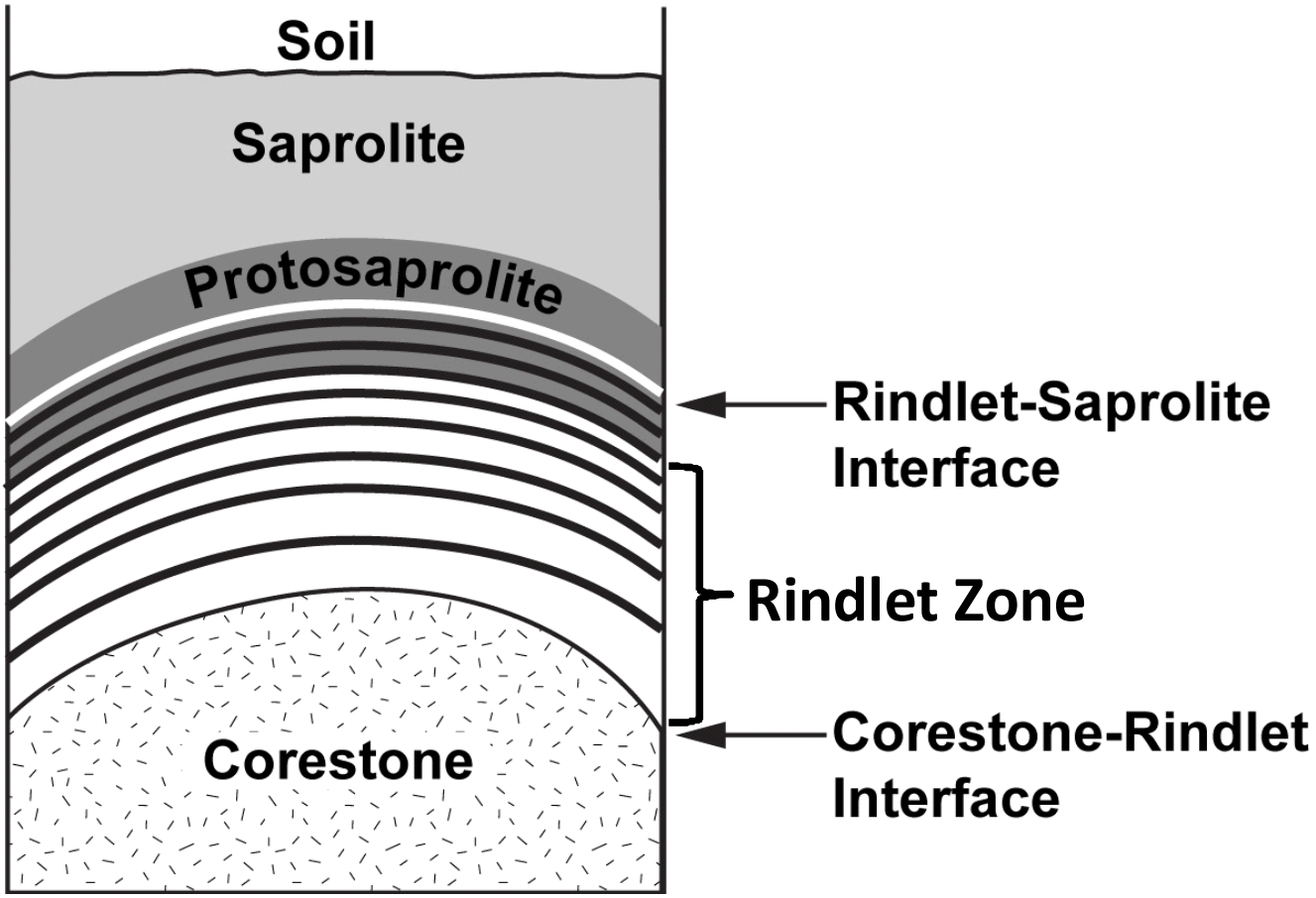
Soil
Saprolite
Protosaprolite
Rindlet-Saprolite Interface
Rindlet Zone
Corestone-Rindlet Interface
Corestone

Figure 2

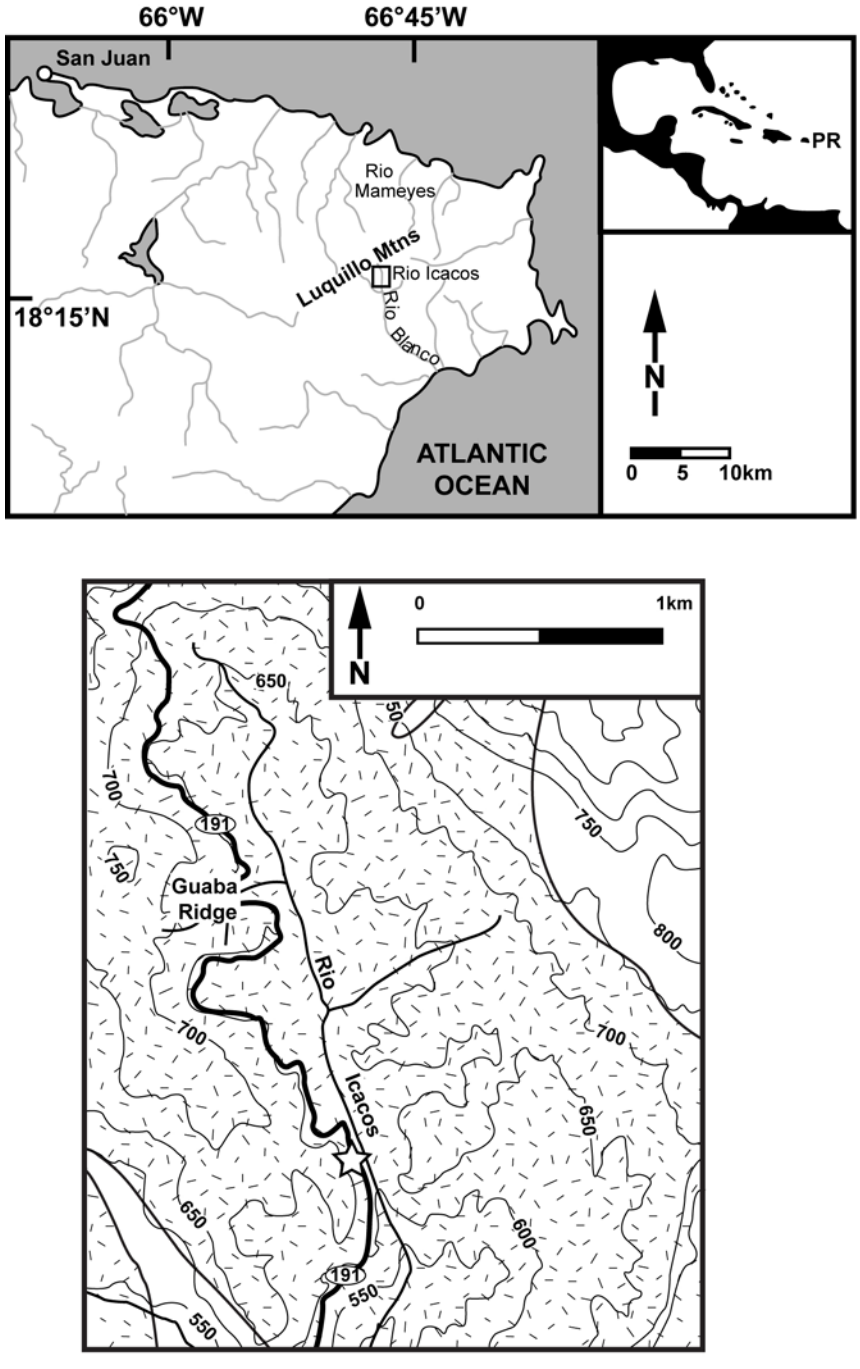
66°W
66°45'W
San Juan
Rio
Mameyes
Luquillo Mtns
Rio Icacos
Rio Blanco
18°15'N
ATLANTIC
OCEAN
PR
N
0 5 10km
0 1km
N
650
700
750
191
Guaba
Ridge
Rio
Icacos
800
600
550

Figure 3

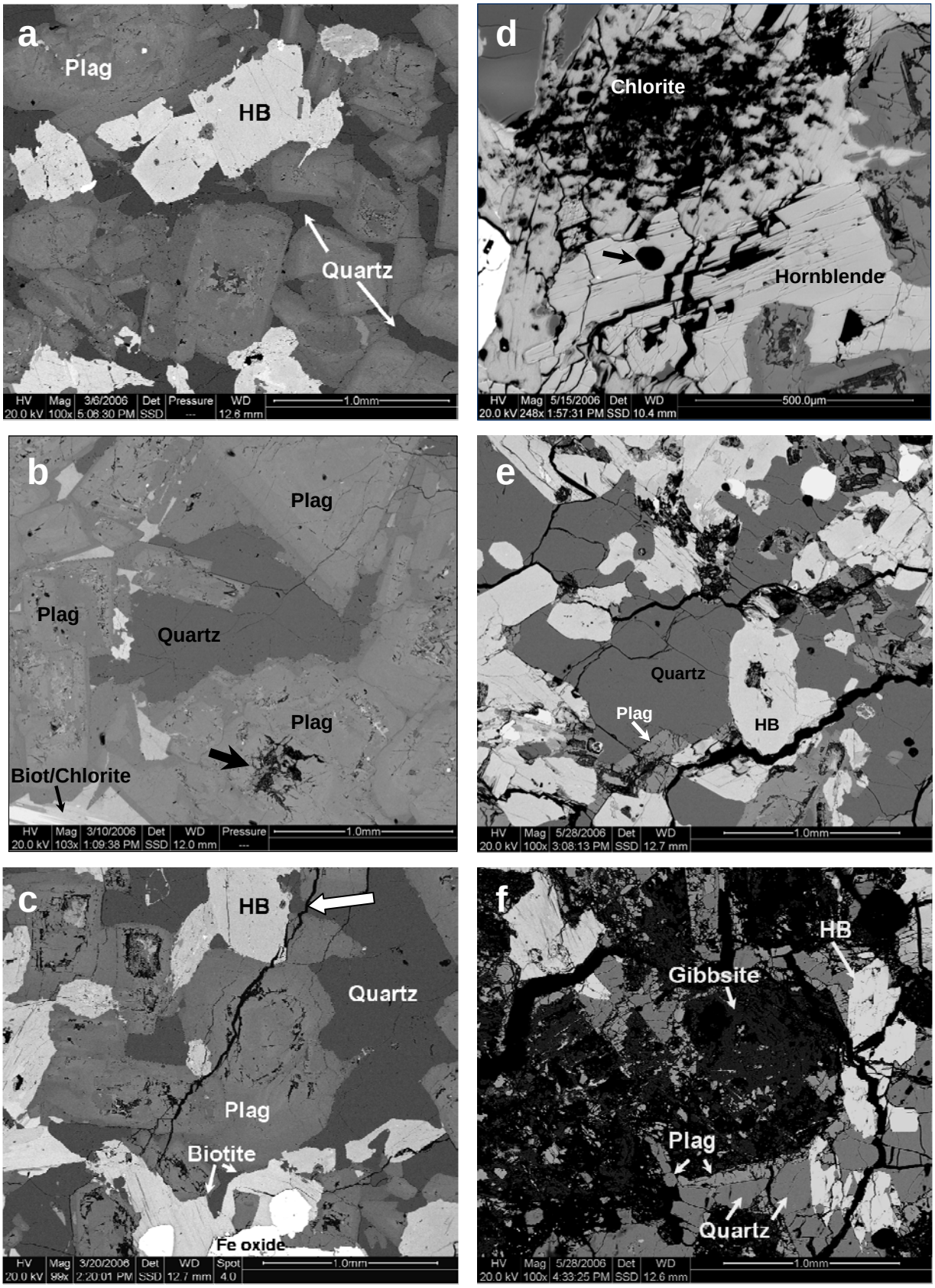
a
Plag
HB
Quartz
HV Mag 3/6/2006 Det Pressure WD 1.0mm
20.0 kV 100x 5:06:30 PM SSD --- 12.8 mm
d
Chlorite
Hornblende
HV Mag 5/15/2006 Det WD 500.0µm
20.0 kV 248x 1:57:31 PM SSD 10.4 mm
b
Plag
Plag
Quartz
Plag
Biot/Chlorite
HV Mag 3/10/2006 Det WD Pressure 1.0mm
20.0 kV 103x 1:09:38 PM SSD 12.0 mm ---
e
Quartz
Plag
HB
HV Mag 5/28/2006 Det WD 1.0mm
20.0 kV 100x 3:08:13 PM SSD 12.7 mm
c
HB
Quartz
Plag
Biotite
Fe oxide
HV Mag 3/20/2006 Det WD Spot 1.0mm
20.0 kV 99x 2:20:01 PM SSD 12.7 mm 4.0
f
HB
Gibbsite
Plag
Quartz
HV Mag 5/28/2006 Det WD 1.0mm
20.0 kV 100x 4:33:25 PM SSD 12.6 mm

Figure 4

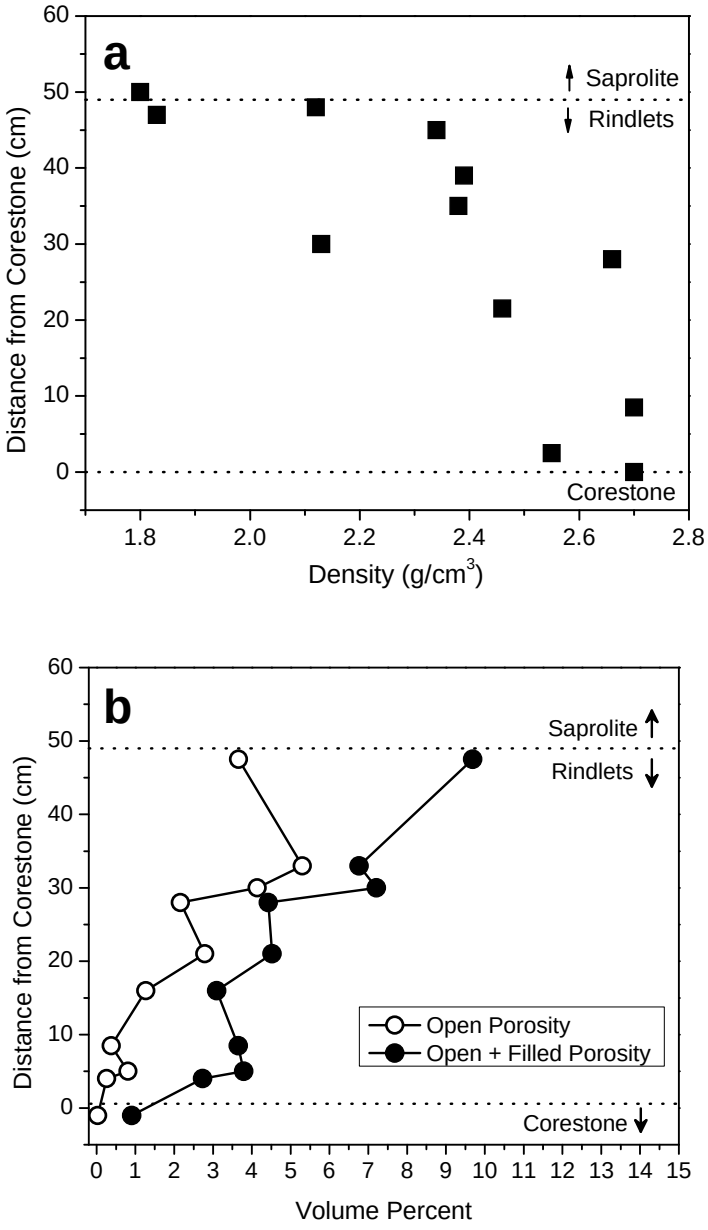
a
Saprolite
Rindlets
Corestone
Distance from Corestone (cm)
Density (g/cm3)
b
Saprolite
Rindlets
Corestone
Open Porosity
Open + Filled Porosity
Distance from Corestone (cm)
Volume Percent

Figure 5

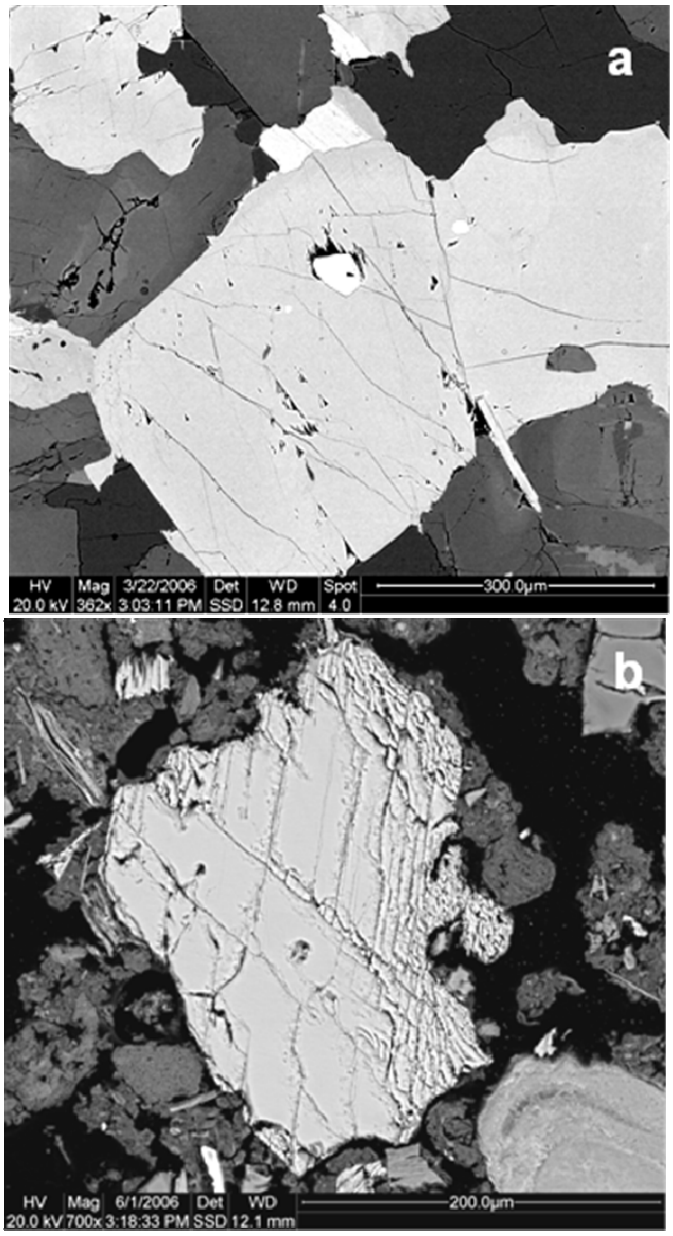
a
HV Mag 3/22/2006 Det WD Spot
20.0 kV 362x 3:03:11 PM SSD 12.8 mm 4.0
300.0µm
b
HV Mag 6/1/2006 Det WD
20.0 kV 700x 3:18:33 PM SSD 12.1 mm
200.0µm

Figure 6

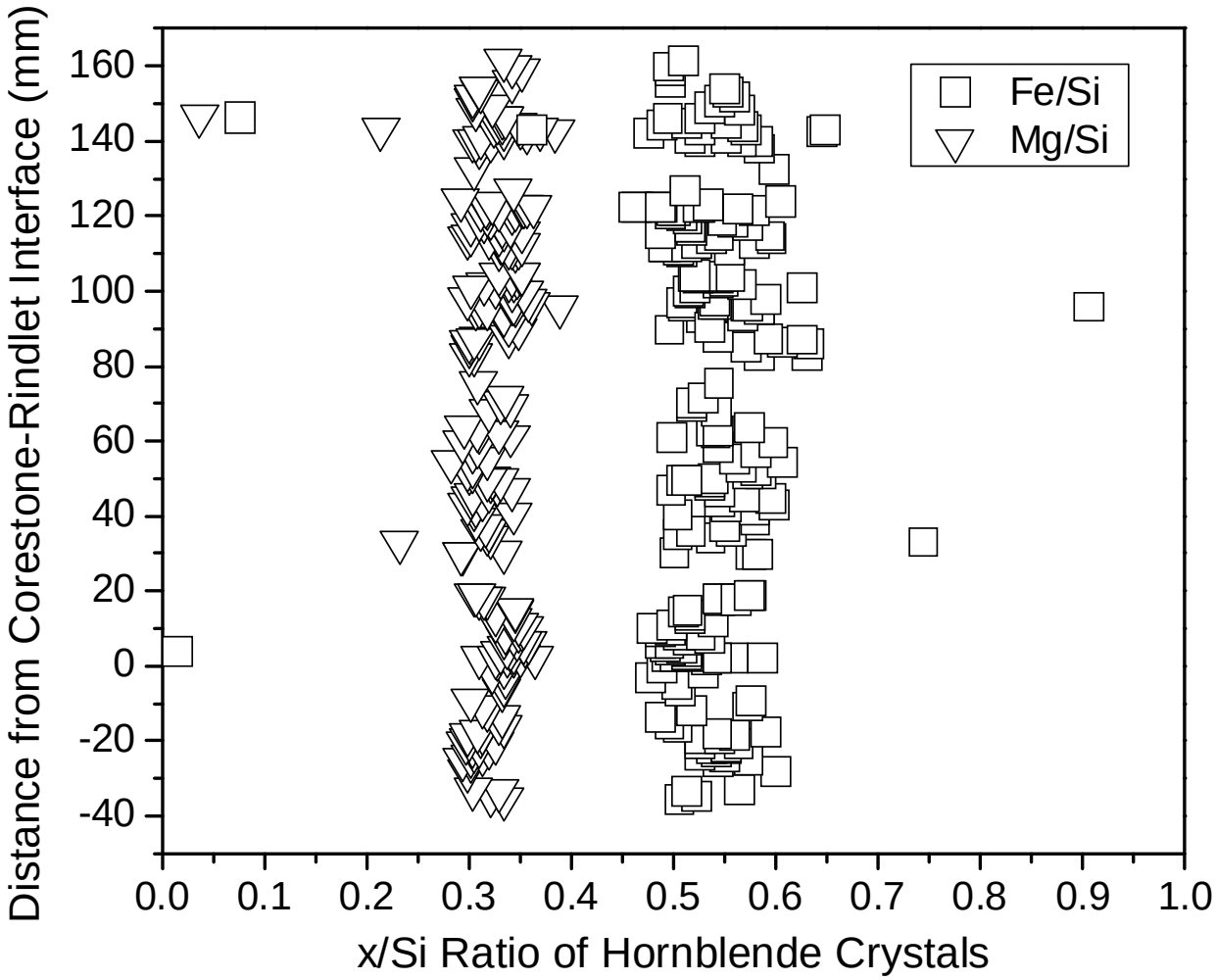
Distance from Corestone-Rindlet Interface (mm)
160
140
120
100
80
60
40
20
0
-20
-40
0.0
0.1
0.2
0.3
0.4
0.5
0.6
0.7
0.8
0.9
1.0
x/Si Ratio of Hornblende Crystals
Fe/Si
Mg/Si

Figure 7

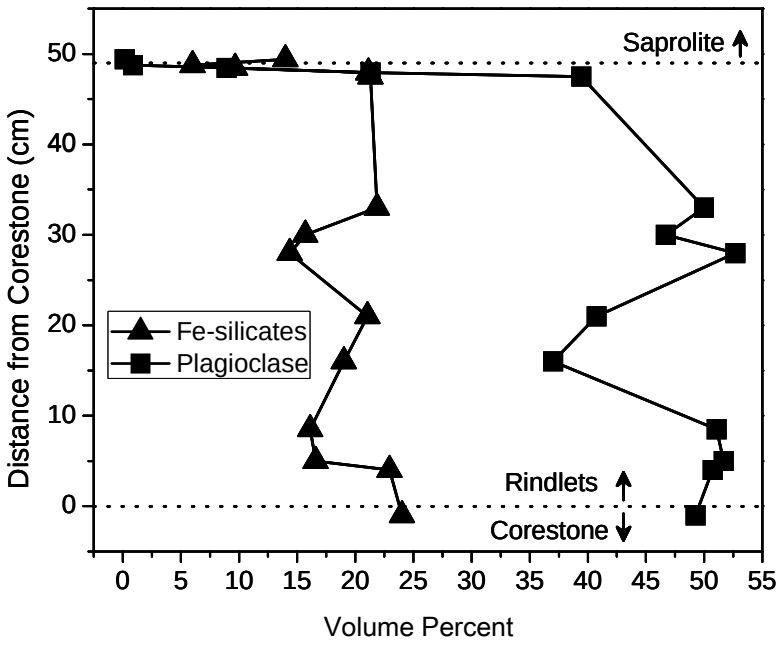
Saprolite
Rindlets
Corestone
Fe-silicates
Plagioclase
Distance from Corestone (cm)
Volume Percent
0
10
20
30
40
50
0
5
10
15
20
25
30
35
40
45
50
55

Figure 8

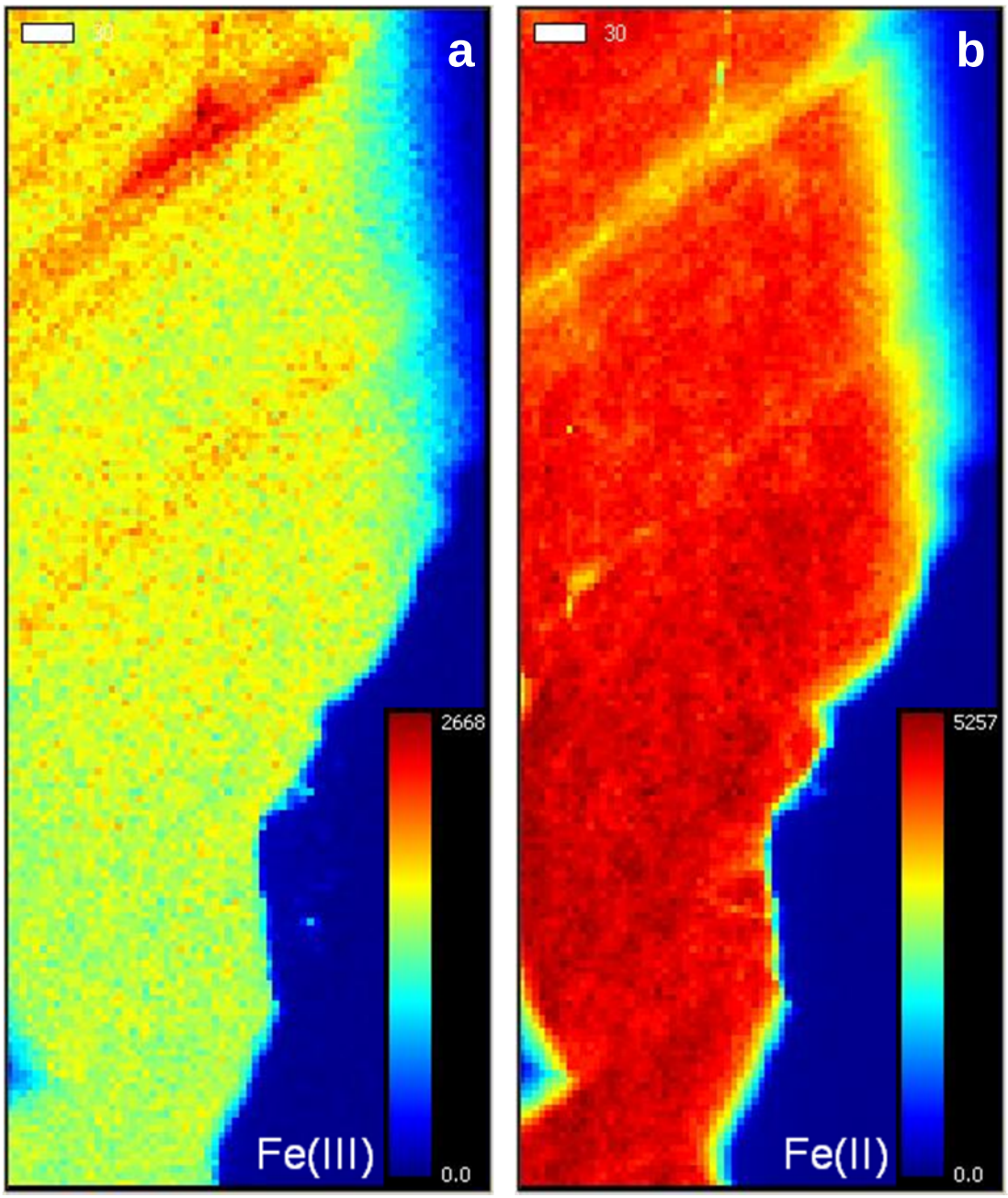


Figure 9

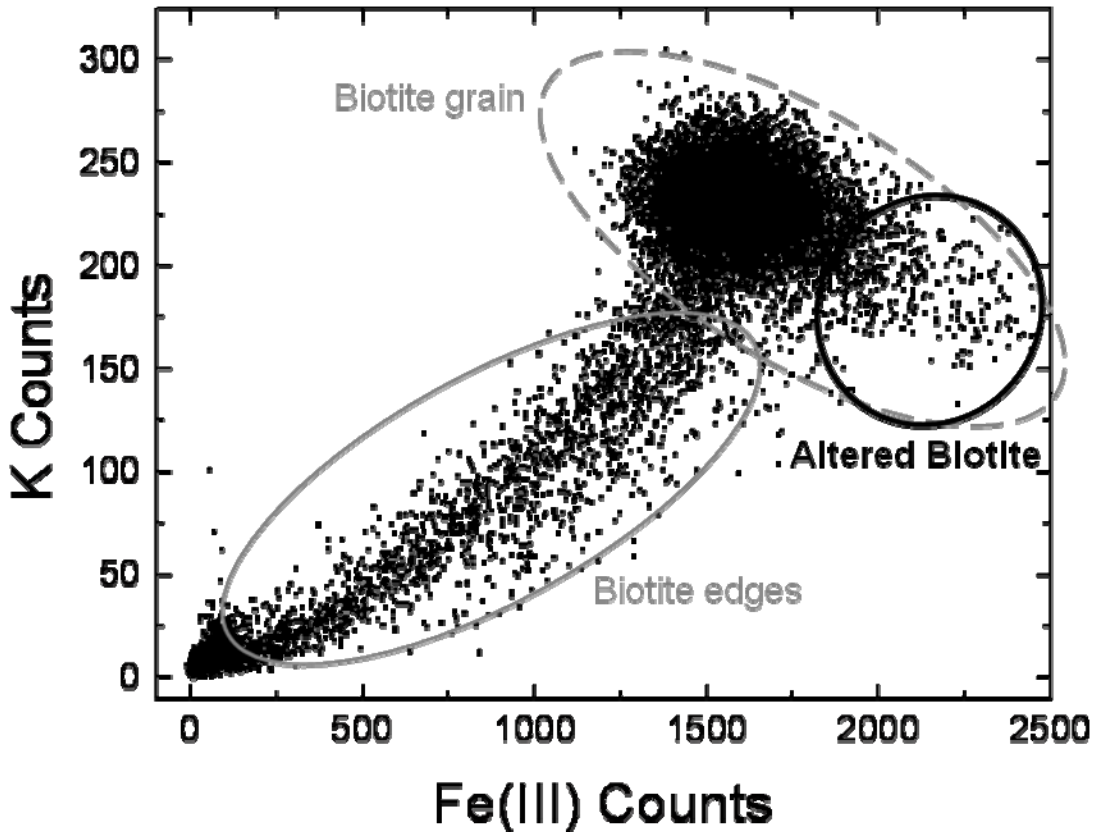
Biotite grain
Altered Biotite
Biotite edges
K Counts
Fe(III) Counts
300
250
200
150
100
50
0
0
500
1000
1500
2000
2500

Figure 10

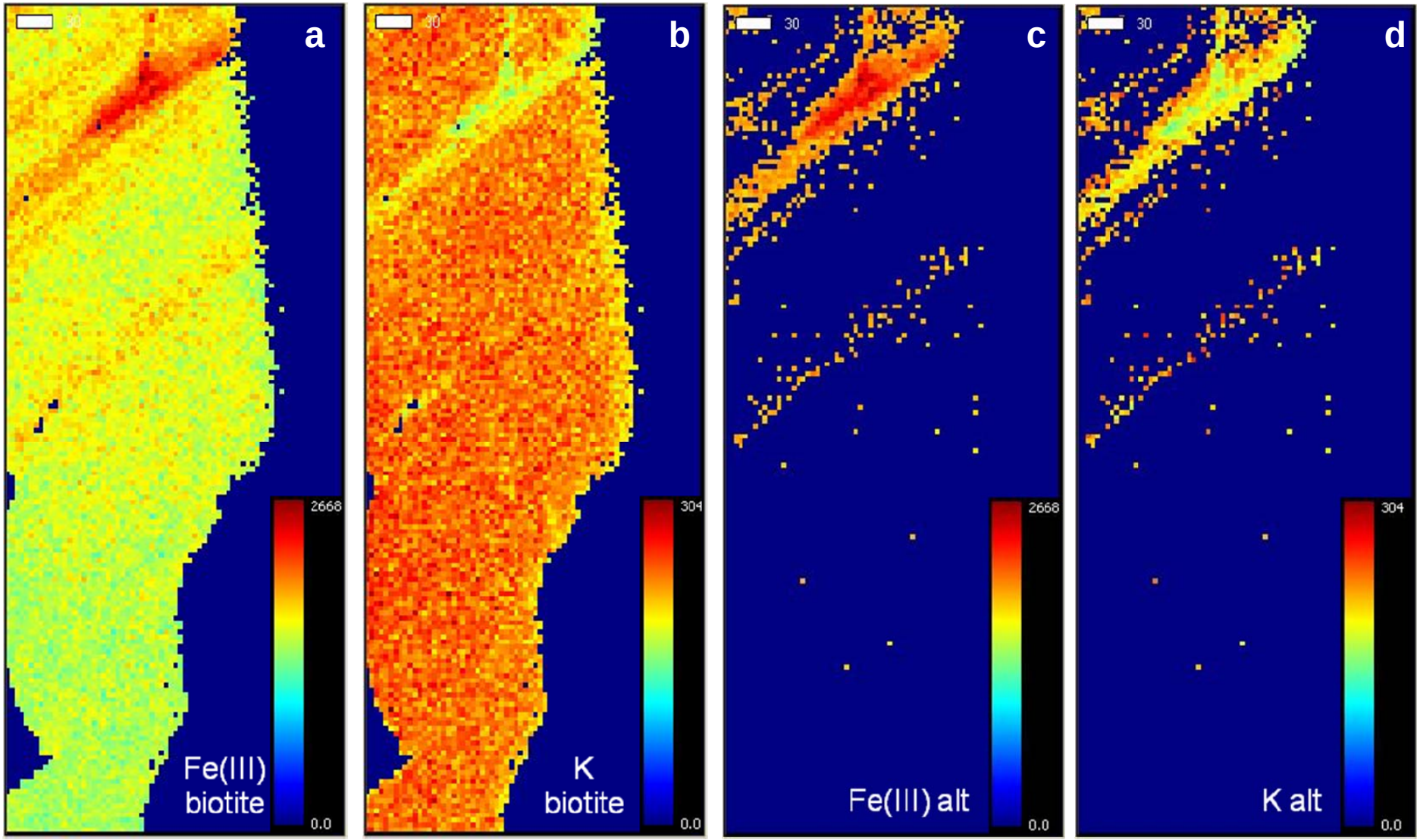
a
30
2668
0.0
Fe(III)
biotite
b
30
304
0.0
K
biotite
c
30
2668
0.0
Fe(III) alt
d
30
304
0.0
K alt

Figure 11

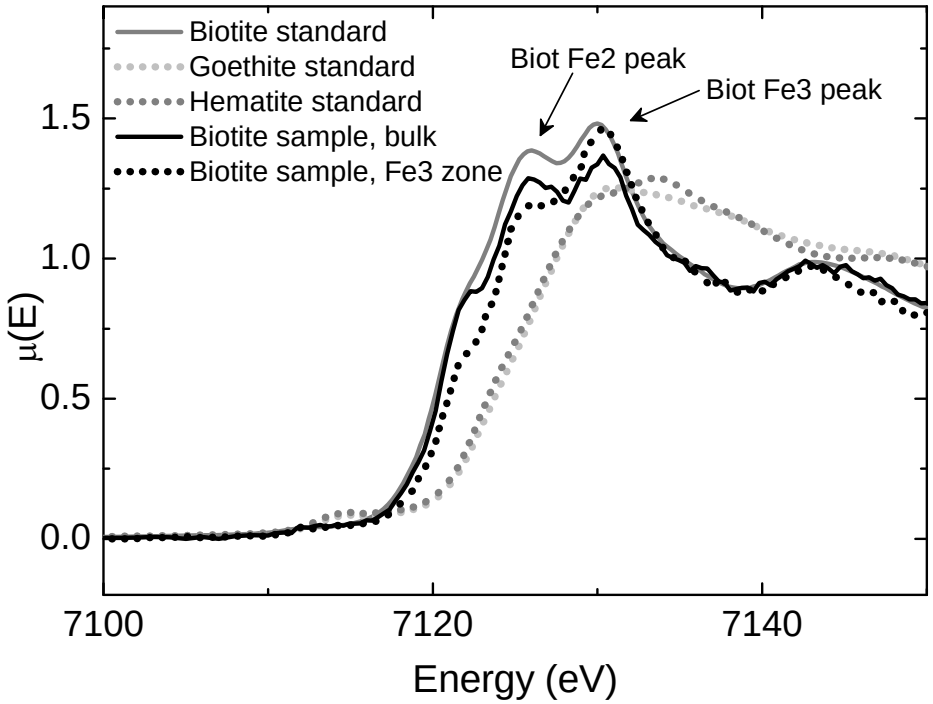
Biotite standard
Goethite standard
Hematite standard
Biotite sample, bulk
Biotite sample, Fe3 zone
Biot Fe2 peak
Biot Fe3 peak
μ(E)
1.5
1.0
0.5
0.0
7100
7120
7140
Energy (eV)

Figure 12

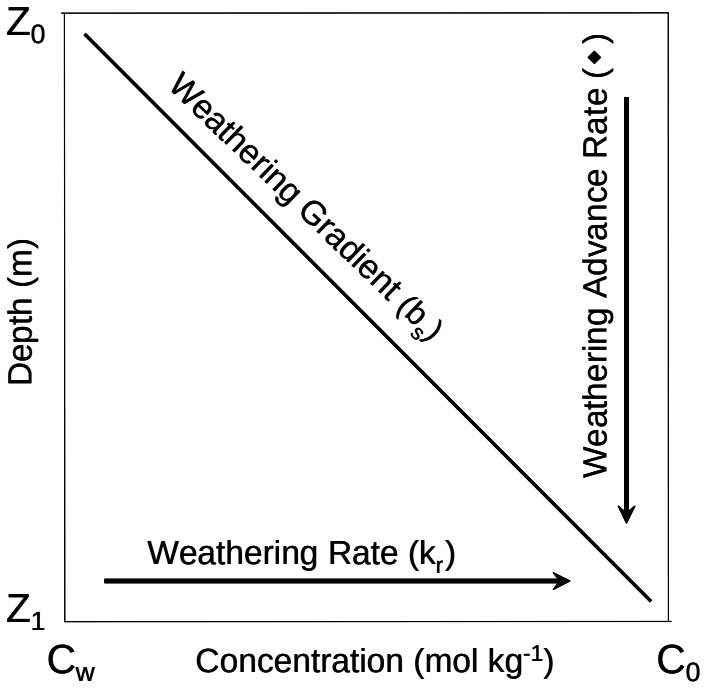
$Z_0$
Depth (m)
$Z_1$
Weathering Gradient ($b_s$)
Weathering Advance Rate (♦)
Weathering Rate ($k_r$)
$C_w$
Concentration (mol $kg^{-1}$)
$C_0$

Figure 13

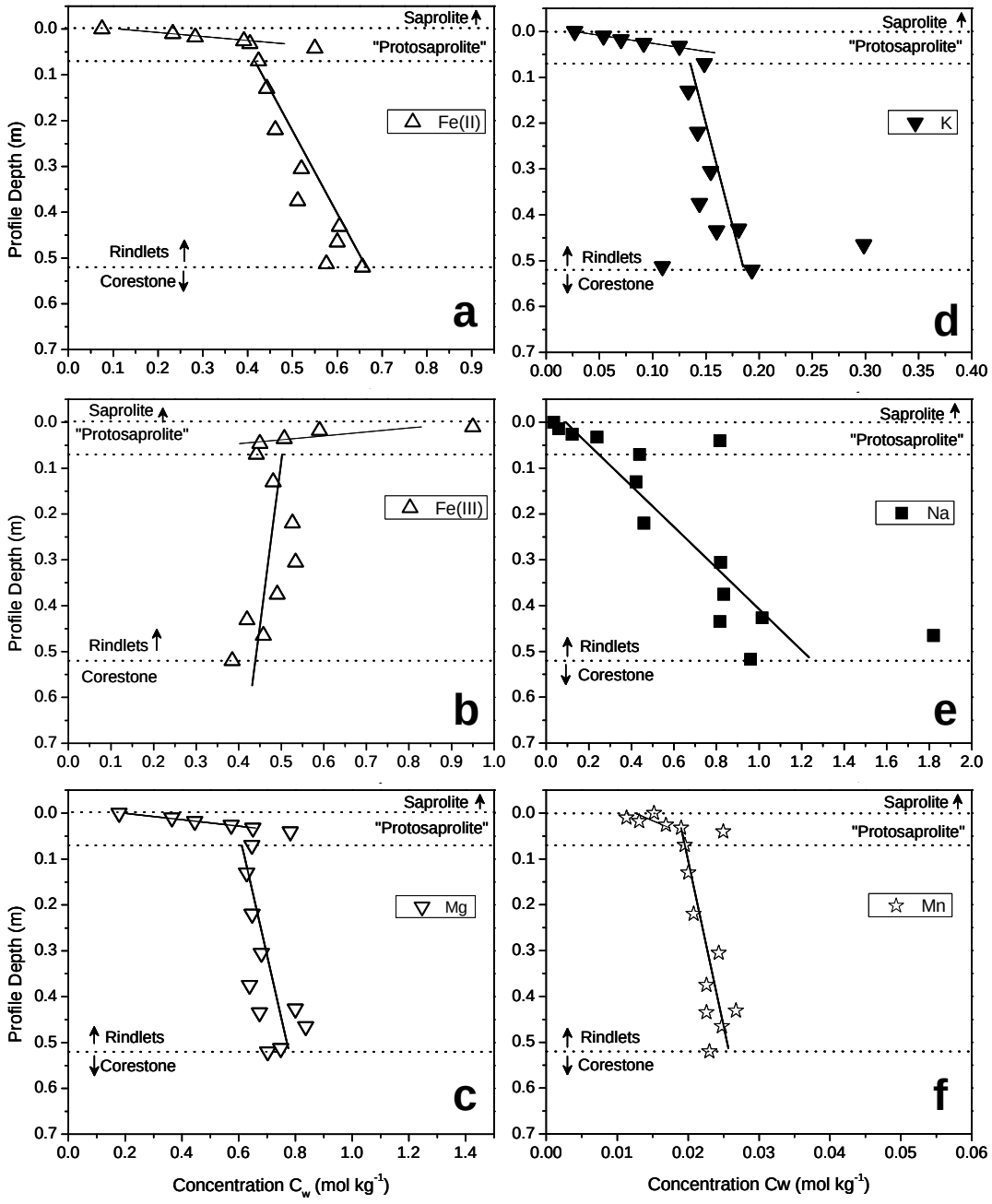
Saprolite
"Protosaprolite"
Fe(II)
Rindlets
Corestone
a
Profile Depth (m)
Saprolite
"Protosaprolite"
K
Rindlets
Corestone
d
Saprolite
"Protosaprolite"
Fe(III)
Rindlets
Corestone
b
Saprolite
"Protosaprolite"
Na
Rindlets
Corestone
e
Saprolite
"Protosaprolite"
Mg
Rindlets
Corestone
c
Concentration $C_w$ (mol $kg^{-1}$)
Saprolite
"Protosaprolite"
Mn
Rindlets
Corestone
f
Concentration Cw (mol $kg^{-1}$)

Figure 14

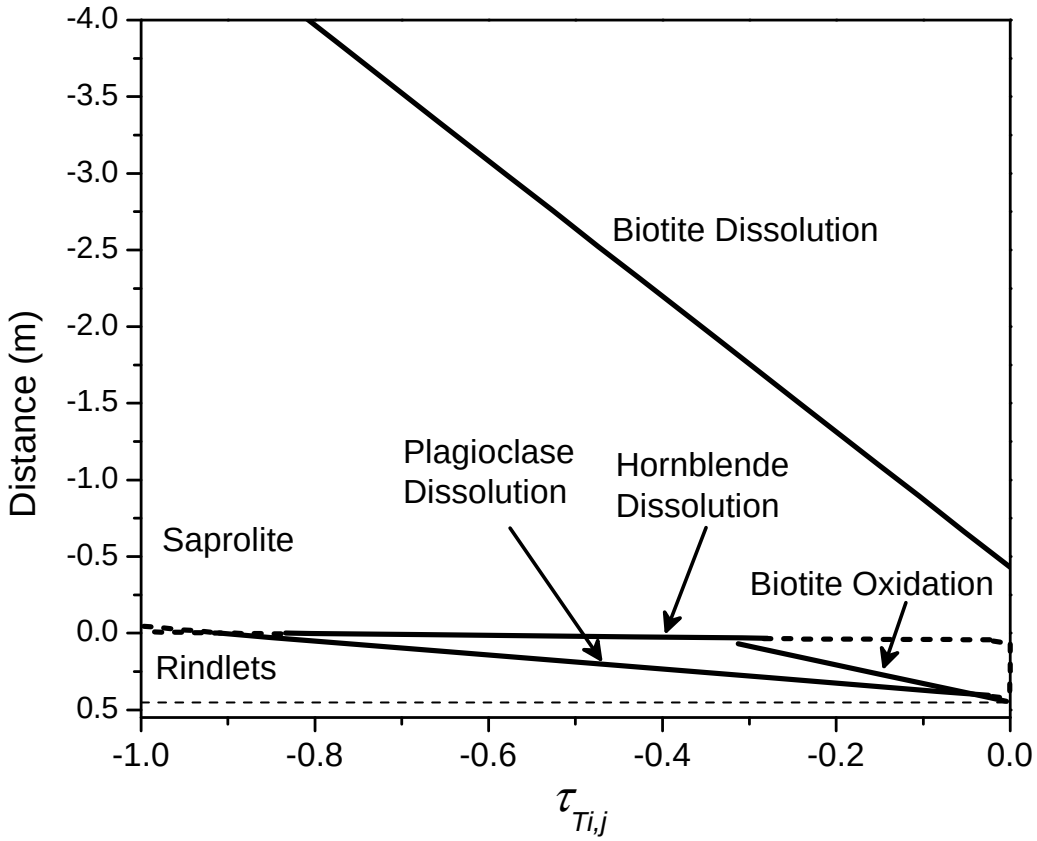
-4.0
-3.5
-3.0
-2.5
-2.0
-1.5
-1.0
-0.5
0.0
0.5
Distance (m)
-1.0
-0.8
-0.6
-0.4
-0.2
0.0
$\tau_{Ti,j}$
Biotite Dissolution
Plagioclase
Dissolution
Hornblende
Dissolution
Saprolite
Biotite Oxidation
Rindlets

Figure 15

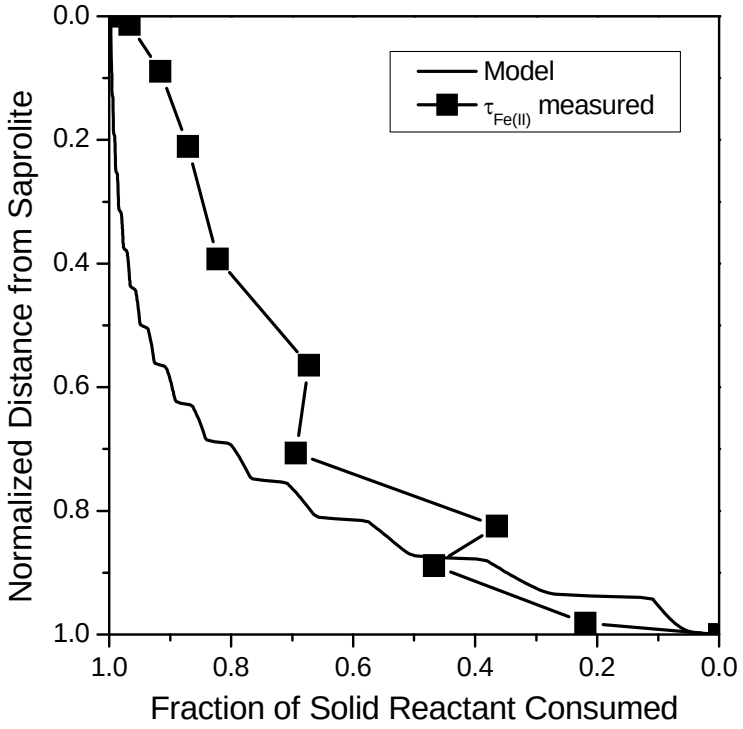
Model
$\tau_{Fe(II)}$ measured
Normalized Distance from Saprolite
0.0
0.2
0.4
0.6
0.8
1.0
1.0
0.8
0.6
0.4
0.2
0.0
Fraction of Solid Reactant Consumed

Figure 16